

# Numerical Relativity Simulations of Dark Matter Admixed Binary Neutron Stars

Edoardo Giangrandi <sup>1,2,\*</sup>, Hannes R. Rüter <sup>3</sup>, Nina Kunert <sup>2,†</sup>, Mattia Emma <sup>4,‡</sup>, Adrian Abac <sup>5,2,§</sup>, Ananya Adhikari <sup>6</sup>, Tim Dietrich <sup>2,5</sup>, Violetta Sagun <sup>7,¶</sup>, Wolfgang Tichy <sup>6</sup> and Constança Providência <sup>1,\*\*</sup>

<sup>1</sup>*CFisUC, Department of Physics, University of Coimbra, Rua Larga P-3004-516, Coimbra, Portugal*

<sup>2</sup>*Institut für Physik und Astronomie, Universität Potsdam, Haus 28, Karl-Liebknecht-Str. 24-25, Potsdam, Germany*

<sup>3</sup>*CENTRA, Departamento de Física, Instituto Superior Técnico – IST,*

*Universidade de Lisboa – UL, Avenida Rovisco Pais 1, 1049-001 Lisboa, Portugal*

<sup>4</sup>*Department of Physics, Royal Holloway University of London, Egham, TW20 0EX*

<sup>5</sup>*Max Planck Institute for Gravitational Physics (Albert Einstein Institute), Am Mühlenberg 1, Potsdam 14476, Germany*

<sup>6</sup>*Department of Physics, Florida Atlantic University, Boca Raton, FL 33431, USA*

<sup>7</sup>*Mathematical Sciences and STAG Research Centre, University of Southampton, Southampton SO17 1BJ, United Kingdom*

(Dated: April 30, 2025)

Binary neutron star mergers provide insight into strong-field gravity and the properties of ultra-dense nuclear matter. These events offer the potential to search for signatures of physics beyond the standard model, including dark matter. We present the first numerical-relativity simulations of binary neutron star mergers admixed with dark matter, based on constraint-solved initial data. Modeling dark matter as a non-interacting fermionic gas, we investigate the impact of varying dark matter fractions and particle masses on the merger dynamics, ejecta mass, post-merger remnant properties, and the emitted gravitational waves. Our simulations suggest that the dark matter morphology - a dense core or a diluted halo - may alter the merger outcome. Scenarios with a dark matter core tend to exhibit a higher probability of prompt collapse, while those with a dark matter halo develop a common envelope, embedding the whole binary. Furthermore, gravitational wave signals from mergers with dark matter halo configurations exhibit significant deviations from standard models when the tidal deformability is calculated in a two-fluid framework. This highlights the need for refined models in calculating the tidal deformability when considering mergers with extended dark matter structures. These initial results provide a basis for further exploration of dark matter's role in binary neutron star mergers and their associated gravitational wave emission and can serve as a benchmark for future observations from advanced detectors and multi-messenger astrophysics.

## I. INTRODUCTION

Following the groundbreaking detection of the first binary neutron star (BNS) merger GW170817 [1], which was accompanied by the detection of its electromagnetic counterparts - the short  $\gamma$ -ray burst GRB170817A, its afterglow, and the kilonova AT2017gfo [2–7] - our understanding of compact stars and their merger dynamics has undergone a significant revolution. This event marked the dawn of gravitational wave (GW) astrophysics for neutron stars (NSs), establishing powerful new tools for probing their internal structure. By combining GW observations with the corresponding electromagnetic signal from the same source, we can now extract information about the properties of matter at its extreme limits [1, 8–11]. The analysis of the GW170817 signal, measured by the advanced LIGO and Virgo detectors, yielded a constraint on the tidal deformability parameter of the  $1.4 M_{\odot}$  NS,  $\Lambda_{1.4} \leq 800$  [12]. Moreover, GW190425 [13], considered a BNS merger candidate, provided constraints

on the equation of state (EOS) of NS matter compatible with those obtained from the first event. However, due to a low signal-to-noise ratio, GW190425 did not provide significant new insights into the specific properties of the EOS [13, 14]. Complementary to the GW observations, X-ray data from NICER [15–19], radio measurements of the heaviest pulsars, i. e., PSR J0348+0432 with a mass of  $2.01 \pm 0.04 M_{\odot}$  [20] and PSR J0740+6620 with  $2.08 \pm 0.07 M_{\odot}$  [21], optical observations of the *black widow* pulsars PSR J1810+1744 with  $2.13 \pm 0.04 M_{\odot}$  [22] and PSR J0952-0607 with  $2.35 \pm 0.17 M_{\odot}$  [23], thermonuclear accretion bursts in low-mass X-ray binaries [24, 25] along with nuclear physics terrestrial experiments provide additional constraints on the properties of NSs and the EOS; see [26] for a recent review. Nevertheless, all the aforementioned analyses and models often employ the simplifying assumption that NSs reside in a perfect vacuum where no dark matter (DM) is present. However, due to the extreme gravitational fields and compactness, NSs might trap and accumulate DM from the galactic halo within their interiors and the surrounding environments. The presence of DM could have a significant impact on the internal structure [27–31], thermal evolution [32], and overall compactness of these objects. The distribution of DM within NSs depends crucially on its particle properties, such as mass, interaction with the Standard Model particles, as well as the amount of trapped DM. Once trapped in the stellar environment,

\* edoardo.giangrandi.1@uni-potsdam.de

† nkunert@uni-potsdam.de

‡ mattia.emma@ligo.org

§ adrian.abac@aei.mpg.de

¶ v.sagun@soton.ac.uk

\*\* cp@uc.pt

DM may either form a dense core in the inner stellar region or be distributed in a diluted halo that completely embeds the baryonic star [33]. In the former case, the increased gravitational pull from the admixed DM leads to more compact NS configurations compared to their purely nucleonic counterparts [32]. On the other hand, a surrounding DM halo can significantly increase the total gravitational mass of the system, pushing the outermost radius of the DM-admixed NS to tens or even hundreds of kilometers [33]. In both scenarios, the presence of the additional DM component may deeply modify the matter distribution, affecting the tidal deformability parameter and causing substantial alterations to BNS merger dynamics and the associated GW signature [34]. The DM fraction accumulated by NSs is highly dependent on their galactic environment. Indeed, NSs located closer to the galactic center or in the DM dense regions are expected to accumulate a greater amount of DM [33]. This is due to the significantly higher DM density present in the center of the galaxy [35, 36]. This spatial dependence on DM density adds another layer of complexity to the potential impact of DM on BNS mergers. Moreover, NSs in binary systems have a particularly long evolutionary timescale, allowing for an even greater DM fraction due to the longer accumulation time and the stronger combined gravitational field of the two stars in a binary system. These factors might lead to higher DM fractions in the NSs in a binary compared to isolated stars [37].

Early investigations into the potential DM influence on the GW signals from BNS mergers include pioneering work such as Ellis *et al.* [34]. They explored the impact of DM cores within NSs on emitted GWs and employed a simplified mechanical model of BNS mergers. Their analysis suggested that DM cores could generate a supplementary peak in the post-merger GW power spectral density, potentially distinguishable from those produced by the Standard Model matter. While providing insights on the possible DM-related features of the GW, the simplified nature of the model may not fully capture the complexity of the merger dynamics, particularly in scenarios involving significant DM fractions, e. g., up to  $\sim 10\%$ , which could need non-standard dark sector models and specific formation scenarios. Bezares *et al.* [38] further investigated GW signatures of BNS mergers with bosonic DM cores using numerical simulations. In their treatment, baryonic matter (BM) was modeled as a perfect fluid and DM as a complex scalar field, with their results indicating the presence of a strong  $m = 1$  mode in the GW waveform. Such an effect was observed only at high boson-to-fermion fractions of 10%. This configuration yielded dark cores causing a mass redistribution, leading to an  $|m| = 1$  over-density via a one-arm instability. However, the overall dynamical evolution and GW signal remained almost unaffected during the merger and inspiral phases, posing a significant challenge to the identification of DM imprints. Bauswein *et al.* [39] modeled NS binaries with a DM component in their interior, approximating DM as test particles within

three-dimensional relativistic simulations. Their simulations suggest that DM remains gravitationally bound within the merger remnant, orbiting inside the BM structure and producing GW signals in the kHz range. Emma *et al.* [40] investigated the merger of BNS systems that contain mirror DM. By performing single-star tests and BNS simulations, their findings suggest that the presence of DM reduces the lifetime of the merger remnant, favoring a prompt collapse to a BH. However the initial data (ID) were constructed using superimposed boosted single-star spacetimes, a simplification that introduces limitations in accurately modeling realistic binary systems. This issue has been addressed by Rüter *et al.* [41], where the SGRID code [42–45] was updated to construct quasi-equilibrium configurations for DM-admixed stars, focusing on the ID problem. Owen *et al.* [46] explored BNS mergers with DM interacting via a massive dark abelian vector field. They calculated modifications to the binary inspiral waveform to the first post-Newtonian order, adding such corrections into a state-of-the-art waveform model. Suárez-Fontanella *et al.* [47] investigated the dynamics in the presence of a viscous DM-polluted environment, using an effective Lagrangian model. The model qualitatively reproduces the GW signal observed in early post-merger phases. While non-viscous DM shows negligible impact on the power spectral density up to a DM fraction of 5%, the inclusion of DM leads to significant damping of the main peak without any frequency shifts. Furthermore, the analysis suggests that this damping could make it difficult for current interferometers to observe key spectral features, which might be mistaken for a prompt collapse. These effects could have implications for the detection and interpretation of GW signals by current and future interferometers, such as LIGO-Virgo-KAGRA, the Einstein Telescope [42, 48–50], Cosmic Explorer [51, 52] and NEMO [53]. To further quantify the DM influence on the BNS coalescence, we present in this work, up to our knowledge, the first consistent simulations using constraint-solved ID of DM-admixed BNS systems. Moreover, we utilize tabulated microphysical EOSs for both fluids, offering a more detailed and realistic model for each component. Another key feature of our simulations is the inclusion of all DM morphologies, including DM halos embedding the stars, which further distinguishes our work from previous studies [40].

The present article is organized as follows. In Section II, we discuss the SGRID code for the ID construction, the BAM code for the time evolution, and the considered BNS configurations. Section III shows the results of this study. We begin by presenting the IDs in (III A), followed by their time evolution in (III B), the fate of the remnant (III C), the angular-velocity evolution (III D), the ejecta masses (III E), and the extracted GWs (III F). Conclusions are presented in Section IV. In Appendix A, we present the time evolution of the L2-norm followed by a discussion of GW convergence in Appendix C.

## II. SETUP

### A. Framework

In this study, we model DM within NSs as a non-interacting fermionic fluid, coupled only through gravity with BM. While acknowledging the possible existence of non-gravitational interactions, we justify this simplification through a combination of observational and experimental constraints. This type of DM model can serve as a simplified framework for exploring GeV to sub-GeV fermionic weakly interacting massive particles, which could describe WIMPs [54], asymmetric DM [29], hidden sector DM [55] or mirror DM scenarios [56]. The observed separation of DM and BM distributions in galaxy clusters collisions, e. g., the Bullet Cluster [57, 58], strongly suggests that DM and BM feebly interact. The observed spatial offset would be significantly smaller if DM and BM had significant non-gravitational interaction. Moreover, direct detection experiments provide an upper limit on the DM-nucleon scattering cross-section which is many orders of magnitude lower than the typical nuclear one [59, 60]. Based on these constraints and considering the very short timescales of the merger, the approximation of no interaction between DM and BM, except through gravity, is fully justified. Therefore, for non-interacting fluids, the energy-momentum tensor can be split into two individual components [40, 61, 62], as

$$T_{\mu\nu}^{(s)} = (\varepsilon^{(s)} + p^{(s)})u_{\mu}^{(s)}u_{\nu}^{(s)} + p^{(s)}g_{\mu\nu}, \quad (1)$$

where the index  $s \in \{\text{BM}, \text{DM}\}$  labels the fluid component,  $\varepsilon$ ,  $p$ , and  $u^{\mu}$  are the energy density, pressure, and the four-velocity of the fluid, respectively.

The Einstein field equations are given by

$$R_{\mu\nu} + \frac{1}{2}g_{\mu\nu}R = 8\pi \sum_s T_{\mu\nu}^{(s)}. \quad (2)$$

Additionally, each of the components satisfies the energy-momentum conservation separately, namely:

$$\nabla^{\mu}T_{\mu\nu}^{(s)} = 0. \quad (3)$$

For each fluid, we can also define the specific enthalpy  $h^{(s)}$

$$h^{(s)} = \frac{\varepsilon^{(s)} + p^{(s)}}{\rho_0^{(s)}}, \quad (4)$$

being computed using the fluid rest-mass density  $\rho_0^{(s)}$ .

### B. Initial data

The initial configurations for the BNS simulations in this work are constructed using the pseudo-spectral code SGRID [42–45]. The SGRID code employs surface fitting coordinates to solve the Einstein constraint equation

through the extended conformal thin sandwich (XCTS) formalism [63, 64]. Using the adapted version of SGRID presented in Ref. [41], DM-admixed BNS configurations are constructed and used as ID for our simulations. The SGRID code deals with the spacetime metric  $g_{\mu\nu}$  using the commonly used 3 + 1 decomposition, where the line element can be written as follows

$$ds^2 = -\alpha dt^2 + \gamma_{ij}(\beta^i dt + dx^i)(\beta^j dt + dx^j), \quad (5)$$

with  $\alpha$ ,  $\beta^i$ , and  $\gamma_{ij}$  being the lapse, shift, and the spatial part of the metric tensor  $g_{\mu\nu}$  induced on three-dimensional spatial hypersurfaces, respectively. The latter can be written down as

$$\gamma_{\mu\nu} = g_{\mu\nu} + n_{\mu}n_{\nu}, \quad (6)$$

with  $n^{\mu}$  being the timelike normal vector to the three-dimensional hypersurfaces defined by

$$n^{\mu} = \frac{1}{\alpha}(1, -\beta^i), \quad \text{and} \quad n_{\mu} = (-\alpha, 0, 0, 0). \quad (7)$$

To generate the initial configurations we assume that the system is in quasi-equilibrium at vanishing temperature,  $T = 0$ . We first solve the equations for the velocity potentials  $\phi^{(s)}$ , which are defined through the following four-velocity

$$\gamma_{\mu}^i u^{(s)\mu} = \frac{1}{h^{(s)}}(D^i \phi^{(s)} + w^{(s)i}), \quad (8)$$

with  $w^{(s)i}$  being a divergence-free vector, representing the rotational part of the fluid component. Following the same approach shown in [41], we can rewrite the final equations derived from Eq. (8) as

$$D_i \left( \frac{\alpha \rho_0^{(s)}}{h^{(s)}}(D^i \phi^{(s)} + w^{(s)i}) - \alpha \rho_0^{(s)} u^{(s)0}(\beta^i + \xi^i) \right) = 0, \quad (9)$$

where the approximate Killing vector  $\xi$  was introduced in order to set the time derivatives of the fields.

To facilitate the convergence of the solver to a physically realistic solution, we construct our initial guess by superimposing two boosted Tolman-Oppenheimer-Volkoff (TOV)-like DM-admixed NSs, each with a specific target mass. Generating ID with the target masses requires determining the central conditions for both fluid components, which is a two-dimensional root-finding problem. This can be easily achieved through an iterative bisection method applied to the central pressure of one fluid while holding the central pressure of the other fluid constant. This process allows us to accurately determine the necessary central pressures to achieve the desired total mass of the two-fluid structure. More advanced iterative algorithms, such as the Newton-Raphson, present challenges as the method may converge to a local extremum of the mass function, effectively halting the iterations. Once the calculated gravitational masses, when computed following Eq. (8) of Ref. [29], are sufficiently

close to the target ones, we evaluate the residuals of Eq. (9). If the latter exceed 10% of the combined residuals of the XCTS equations [65, 66], we solve Eq. (9). Subsequently, we update the four-velocity by taking a weighted average of the previous solution  $\phi_{\text{old}}^{(s)}$  and the newly obtained one  $\phi_{\text{new}}^{(s)}$  as

$$\phi^{(s)} = w\phi_{\text{old}}^{(s)} + (1 - w)\phi_{\text{new}}^{(s)}. \quad (10)$$

In this iterative process,  $w$  represents a weighting factor designed to reduce the accumulation of numerical errors and to enhance the constructed ID's reliability and accuracy. To achieve a suitable balance between considering new information and preserving numerical stability, we set  $w = 0.85$ , reducing the chances of overshooting during the iteration process [67]. Once the newly updated four-velocity is obtained, we solve the XCTS equations, updating the values of  $\alpha$ ,  $\beta$ , and the conformal factor  $\psi$ , using the same weighted average between the old and new solutions.

After adjusting the values of  $h^{(s)}$  to obtain the correct target masses for both fluids, the algorithm checks for convergence. If the sum of the residuals is smaller than a user-chosen threshold or if the number of iterations reaches a prescribed limit, the algorithm stops. Then a final solution of the XCTS equations is computed. However, if the ID has not converged properly, SGRID repeats the entire procedure from the evaluation of the residuals of Eq. (9).

To close the system, EOSs are needed, either as the parameters of piecewise polytropes or as full tabulated EOSs. The tabulated EOSs are then interpolated in SGRID in a thermodynamically consistent way using a cubic Hermite interpolation. The considered BM and DM EOSs are discussed in Section IID.

Another important aspect of the SGRID code is that it uses surface-fitting coordinates. This approach is designed to avoid (or reduce) numerical Runge oscillations [68]. These oscillations arise when using high-degree polynomial interpolations to approximate functions describing the star's physical properties, such as density or pressure. This phenomenon leads to physical inaccuracies, particularly near the surface of the star, where the solution is not smooth. With each update to the specific enthalpy  $h^{(s)}$ , the computational grid is adapted to ensure that the boundaries of the spectral elements align with the new outer fluid surface. In our current implementation, surface fitting is adapted to binary systems and does not allow fluid surfaces that overlap, e.g., DM-halo common envelope. Furthermore, we do not construct domains that are fitted to the surface of the inner fluid and hence the Runge phenomenon is expected to be observed at the surface of the inner fluid. Extending the code's capabilities to handle more complex scenarios, such as a DM common envelope in the ID, would necessitate a substantial restructuring of the computational framework.

### C. Dynamical Evolution

The BAM code is used for the dynamical evolution of the matter and spacetime fields [69–76]. The code solves Einstein's field equations exploiting the 3 + 1 decomposition, cf. Section IIB. In the presented runs, the Z4c formulation of the field equations of General Relativity with constraint damping terms [77–81], coupled with the moving puncture gauge 1 + log-slicing and gamma-driver shift conditions [82], was employed for the spacetime evolution.

This work focuses on ideal general-relativistic hydrodynamics (GRHD) simulations, excluding magnetic fields and neutrino interaction. In our two-fluid approach to model DM and BM within the numerical simulations, we represent each component as a separate fluid that exists in the same space domain. Within this framework, matter variables are evolved using the Valencia formulation [83]. The evolution equations for ideal GRHD are derived from the conservation laws of particle number and energy-momentum:

$$\nabla_{\mu}(\rho^{(s)}u^{(s)\mu}) = 0, \quad \text{and} \quad \nabla_{\mu}T^{(s)\mu\nu} = 0, \quad (11)$$

with  $\nabla_{\mu}$  being the covariant derivative. To write the evolution system in the form of a balance law as

$$\frac{\partial \mathbf{q}^{(s)}}{\partial t} + \frac{\partial \mathbf{F}^{(s)i}}{\partial x^i} = \mathbf{s}^{(s)}, \quad (12)$$

we define the primitive hydrodynamic variables,  $\mathbf{w}^{(s)} = [p^{(s)}, \rho^{(s)}, \varepsilon^{(s)}, v^{(s)i}]$ , and the conservative variables  $\mathbf{q}^{(s)} = [D^{(s)}, S_i^{(s)}, \tau^{(s)}]$ :

$$D^{(s)} = \sqrt{\gamma}\rho^{(s)}W^{(s)}, \quad (13)$$

$$S_i^{(s)} = \sqrt{\gamma}W^{(s)2}h^{(s)}\rho^{(s)}v_i^{(s)}, \quad (14)$$

$$\tau^{(s)} = \sqrt{\gamma}(W^{(s)2}h^{(s)}\rho^{(s)} - p^{(s)}) - D^{(s)}, \quad (15)$$

where  $\gamma$  is the determinant of the spatial metric  $\gamma_{ij}$  of the 3 + 1 decomposition of the spacetime,  $\rho^{(s)}$  the rest mass density and  $W^{(s)}$  is the Lorentz factor relative to the Eulerian observer. We can obtain the evolution equations in the form of Eq. (12):

$$\mathbf{q}^{(s)} = [D^{(s)}, S_i^{(s)}, \tau^{(s)}], \quad (16)$$

$$\mathbf{F}^{(s)i} = \alpha \begin{bmatrix} D^{(s)}\tilde{v}^{(s)i} \\ S_j^{(s)}\tilde{v}^{(s)i} + \sqrt{\gamma}p^{(s)}\delta_j^i \\ \tau^{(s)}\tilde{v}^{(s)i} + \sqrt{\gamma}p^{(s)}v^{(s)i} \end{bmatrix}, \quad (17)$$

$$\mathbf{s}^{(s)} = \alpha\sqrt{\gamma} \begin{bmatrix} 0 \\ T^{(s)\mu\nu} \left( \frac{\partial g_{\nu j}}{\partial x^{\mu}} - \Gamma_{\mu\nu}^{\lambda}g_{\lambda j} \right) \\ \alpha \left( T^{(s)\mu 0} \frac{\partial \ln(\alpha)}{\partial x^{\mu}} - T^{(s)\mu\nu}\Gamma_{\mu\nu}^0 \right) \end{bmatrix}, \quad (18)$$

where  $\tilde{v}^{(s)i} = v^{(s)i} - \beta^i/\alpha$  and  $\Gamma_{\mu\nu}^{\lambda}$  are the Christoffel symbols.

## D. BM and DM EOSs

For both components, we employ zero-temperature tabulated EOSs. BM is modeled with the SLy4 EOS [84], which supports isolated NSs with the maximum gravitational mass of  $2.06M_{\odot}$ , with a radius  $R_{M_{\max}} = 10.02$  km. We note that SLy4 EOS, being relatively soft, is able to support NSs with tidal deformabilities  $\tilde{\Lambda} \sim 400$  for a  $1.35M_{\odot}$  NS, consistent with current observations and constraints [85]. The SLy4 EOS is selected due to its established and widespread use within the NR community. BM thermal effects are taken into account as prescribed in [86, 87] with the thermal contribution to the total pressure modeled as  $p_{\text{th}}^{(s)} = (\Gamma_{\text{th}}^{(s)} - 1)\rho^{(s)}\varepsilon_{\text{th}}^{(s)}$ . In our simulations, we use a thermal adiabatic index  $\Gamma_{\text{th}}^{(\text{BM})} = 1.75$ .

DM is modeled as a non-interacting fermionic gas of massive particles with spin 1/2 and particle mass  $m_{\text{DM}}$  [33, 41, 88]. DM is treated as isothermal, with a thermal adiabatic index of  $\Gamma_{\text{th}}^{(\text{DM})} = 1$ , resulting in  $p_{\text{th}}^{(s)} = 0$ , so that thermal contributions of DM to the pressure are neglected. Moreover, to analyze the effect of the morphology of the DM structure on the dynamics of the merger, we select two particle masses for our simulations: 1 GeV and 0.17 GeV. These values are consistent with those extensively discussed in the literature for producing different DM halos and cores [33, 41, 88]. Within this framework, we define the DM fraction by exploiting the gravitational masses of the fluids as

$$f_{\text{DM}} = \frac{M^{(\text{DM})}}{M^{(\text{BM})} + M^{(\text{DM})}}, \quad (19)$$

where  $M^{(s)}$  is the gravitational mass of the fluid  $s$ .

## E. Atmosphere

In grid-based numerical relativity (NR) simulations, an artificial atmosphere is typically introduced in the vacuum region surrounding compact objects. This is due to the fact that extremely low rest-mass densities pose a significant numerical challenge, potentially leading to inaccuracies in the recovery of the primitive variables and within high-resolution shock-capturing schemes [89, 90]. Our artificial atmosphere is implemented as a cold static fluid. The density within the atmosphere for each fluid is set to a fraction  $f_{\text{atm}}$  of the initial maximum density as  $\rho_{\text{atm}}^{(s)} = f_{\text{atm}} \max_{\mathbb{R}^3} \rho^{(s)}(t=0)$ . The atmosphere pressure and internal energy are then determined using the zero-temperature part of each EOS, while the fluid velocity is set to zero. To prevent fluctuations near the density floor, we define a threshold density,  $\rho_{\text{th}}^{(s)} = f_{\text{th}}\rho_{\text{atm}}^{(s)}$ , in terms of the fraction  $f_{\text{th}}$  of the atmospheric density [70]. Within the BAM code, we set a grid cell to atmosphere when its density falls below such a threshold. For the BNS runs presented in Section III, we use  $f_{\text{atm}} = 10^{-11}$  and  $f_{\text{th}} = 10$  for the BM and DM components.

## F. Grid setup

The BAM code employs cell-centered nested grids with  $L$  refinement levels, indexed by  $\ell = 0, \dots, L-1$ . Each level contains one or more boxes defined by a constant grid spacing  $h_{\ell}$  and  $n$  points per direction. A 2-to-1 refinement strategy ensures that the resolution in each level is given by  $h_{\ell} = h_0/2^{\ell}$ . Finer levels with  $\ell \geq \ell_{\text{move}}$  move dynamically, tracking the motion of the NSs or black holes (BHs) [69–71, 91]. In this work, we used  $\ell = 7$  or  $\ell = 8$  for DM-core (halo) configurations and  $\ell_{\text{move}} = 2$ . This choice was motivated by the necessity of fully enclosing the stars within the finest grid level, especially for the DM-halo configurations, which have significantly larger outermost radii compared to the core configurations. Thus, in all cases, the outer fluid, either DM (for DM-halo configurations) or BM (for DM-core configurations), was entirely contained within the highest refinement level. This ensured a reliable resolution for a meaningful comparison between the two scenarios. We simulated three distinct resolutions R1, R2, and R3, corresponding to 96, 144, and 192 grid points per direction at the finest level, respectively. The non-moving grids have the following number of grid points  $R1_{\text{NM}} = 128$ ,  $R2_{\text{NM}} = 192$  and  $R3_{\text{NM}} = 256$ . The levels consist of two boxes that individually enclose each star. For all moving levels, boxes are created around each object; when these boxes overlap, a single bounding box is formed. In this work, we employ the method of lines with a fourth-order Runge-Kutta scheme and a Berger-Oliger algorithm for the refinement levels for the time evolution [92, 93]. The spacetime part utilizes a finite difference scheme with centered fourth-order stencils to compute spatial derivatives. Hydrodynamical variables are represented by a finite volume formalism, incorporating high-resolution shock-capturing schemes to calculate numerical fluxes between cells. We use WENOZ [94] reconstruction of characteristic fields together with the LLF Riemann solver. Furthermore, the conservative adaptive mesh refinement strategy, as outlined in [71], was used for both fluids to ensure the conservation of baryonic mass, energy, and momentum.

## III. RESULTS

This section presents the main results of our NR simulations exploring the properties of non-interacting fermionic DM-admixed BNS mergers. We focus on the impact of the DM component on the key features of such phenomena, including IDs (Section III A), time evolution of such systems (Section III B), angular-velocity profiles (Section III D), remnant properties (Section III C), ejecta masses (Section III E), and the extracted GW (Section III F).

### A. Initial Data

We run a total of six different DM-admixed BNS configurations, summarized in Table I. To better study how the DM impacts the remnant fate, we choose two different total masses  $2.8M_{\odot}$  and  $2.4M_{\odot}$ , but restrict to equal mass and irrotational setups. We identify these setups as M28 and M24 in the text, respectively. Regarding the DM content, we choose three different DM fractions, namely 0% (purely baryonic), 0.5% for DM halos, and 3% for DM cores. These choices ensure that the outer fluid components of the DM-admixed NSs do not overlap, avoiding the formation of a common DM envelope in the ID. We note that the chosen DM fractions represent a significant amount of DM and are intentionally selected as an extreme case to highlight potential DM effects in these scenarios. All IDs are constructed using the updated SGRID code, employing the two-fluid formalism. For purely baryonic configurations we specifically set the DM component to zero. Achieving physically realistic and acceptably low eccentricities, such as  $\epsilon \lesssim 10^{-3}$ , proves difficult in these DM-free cases. This issue arises from limitations within the two-fluid SGRID branch that lacks of a stabilizing mechanism that prevents the stars from drifting apart during each iteration. However, the exact source of these difficulties requires further investigation. This problem is exacerbated when the stars are close to each other. For ID affected by this problem, the stars plunge towards each other, when evolved with the BAM code, thus hindering our ability to reduce the orbital eccentricity. To ensure stable and physically meaningful initial conditions, we opted for a larger initial separation  $d_{\text{in}}$  in the DM-free simulations. Furthermore, we evaluate the tidal deformability of the IDs, following the standard prescription outlined in [29, 95]. Within our two-fluid formalism, the tidal deformability  $\Lambda$  is computed by integrating Love’s ordinary differential equation [96] up to the outermost radius  $R_{\text{out}}$ , which is defined as the BM radius (for DM-core configurations) or the DM one (for DM-halo configurations).

### B. Evolution

Figure 1 shows the evolution of the central rest-mass density of BM and DM for the M24 simulations presented here. Before the merger, defined as the point at which the GW amplitude reaches its peak value, we observed minor initial transient density oscillations in both fluids. These transients could arise from the interpolation of the ID, from the approximate choice of the free data in the XCTS equations, and from the absence of surface-fitting coordinates within SGRID for the inner fluid. Right before the merger, the central densities of both the BM and DM components experience a slight decrease as the binary separation shrinks. This effect is due to the increasing tidal forces, which stretch the stars, resulting in a lower maximum density. All simulations reach a sta-

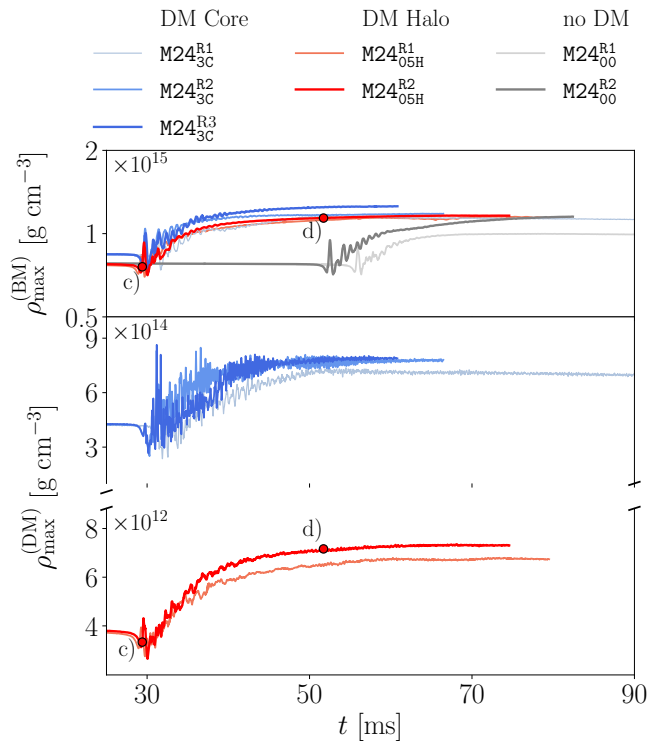


FIG. 1. Comparison of the central rest-mass densities during the merger and post-merger phase for BM (upper panel) and DM (lower panel) for the systems with the total gravitational mass of  $2.4M_{\odot}$ . The central rest-mass density is extracted from the finest refinement level in each run. The points labeled with letters indicate the specific times that correspond to the 2D slices shown in Fig. 2.

ble post-merger configuration. In simulations with DM cores, the presence of DM within the remnant leads to an increased gravitational pull compared to the DM-free runs. This yields more compact remnants with higher central BM densities. On the other hand, while DM halos still impact the overall merger dynamics, their gravitational effect on the central region is less pronounced. The halo contributes to the total gravitational mass of the system, affecting the orbital evolution and the merger time. However, it does not significantly affect the matter distribution of the remnant, showing that the overall effect on BM is minimal. To further examine the dynamics and better visualize the merger, we select two key time points ( $c$ ,  $d$ ) in Figure 1 that correspond to the 2D bottom panels shown in Figure 2. These points represent different stages of the merger:  $c$ ) the merger time, and  $d$ ) the post-merger phase, showing the hypermassive NS (HMNS) remnant. Figure 2 shows the spatial distribution of the rest-mass density for both BM ( $\rho^{(\text{BM})}$ ) and DM ( $\rho^{(\text{DM})}$ ) in the M24<sub>05H</sub><sup>R2</sup> run, where DM extends beyond the BM component, forming dilute DM halos. At  $t - t_{\text{m}} = -28.7$  ms ( $t_{\text{m}}$  being the merger time), panel  $a$ ) of Figure 2, the simulation shows the two DM-admixed NSs in the early inspiral phase. The initial central BM density within

ID	$m_{\text{DM}}$ [GeV]	$f_{\text{DM}}$ [%]	$M_{\text{TOV}}$ [ $M_{\odot}$ ]	$M_{\text{ADM}}$ [ $M_{\odot}$ ]	$J_{\text{ADM}}$ [ $M_{\odot}$ ]	$R^{(\text{BM})}$ [km]	$R^{(\text{DM})}$ [km]	$d_{\text{in}}$ [km]	$\Lambda^{\text{out}}$	DM Morphology
M24 <sub>00</sub>	-	0	2.40	2.382	6.39	11.400	-	53.05	818	None
M24 <sub>3C</sub>	1	3	2.40	2.381	6.08	11.154	5.329	47.02	730	Core
M24 <sub>05H</sub>	0.17	0.5	2.40	2.381	6.09	11.377	18.645	46.91	2908	Halo
M28 <sub>00</sub>	-	0	2.80	2.778	8.38	11.407	-	56.02	310	None
M28 <sub>3C</sub>	1	3	2.80	2.774	7.91	11.143	5.122	47.07	234	Core
M28 <sub>05H</sub>	0.17	0.5	2.80	2.774	7.86	11.379	16.575	46.98	901	Halo

TABLE I. Table of DM-admixed BNS parameters of the IDs. From left to right: ID, DM particle mass  $m_{\text{DM}}$ , DM mass fraction  $f_{\text{DM}}$ , total gravitational mass  $M_{\text{TOV}}$ , ADM mass  $M_{\text{ADM}}$ , ADM angular momentum  $J_{\text{ADM}}$ , TOV BM radius  $R^{(\text{BM})}$ , TOV DM radius  $R^{(\text{DM})}$ , the initial orbital separation  $d_{\text{in}}$  and the tidal deformability  $\Lambda^{\text{out}}$  calculated using the outermost radius following Ref. [29, 97], and DM morphology, respectively.

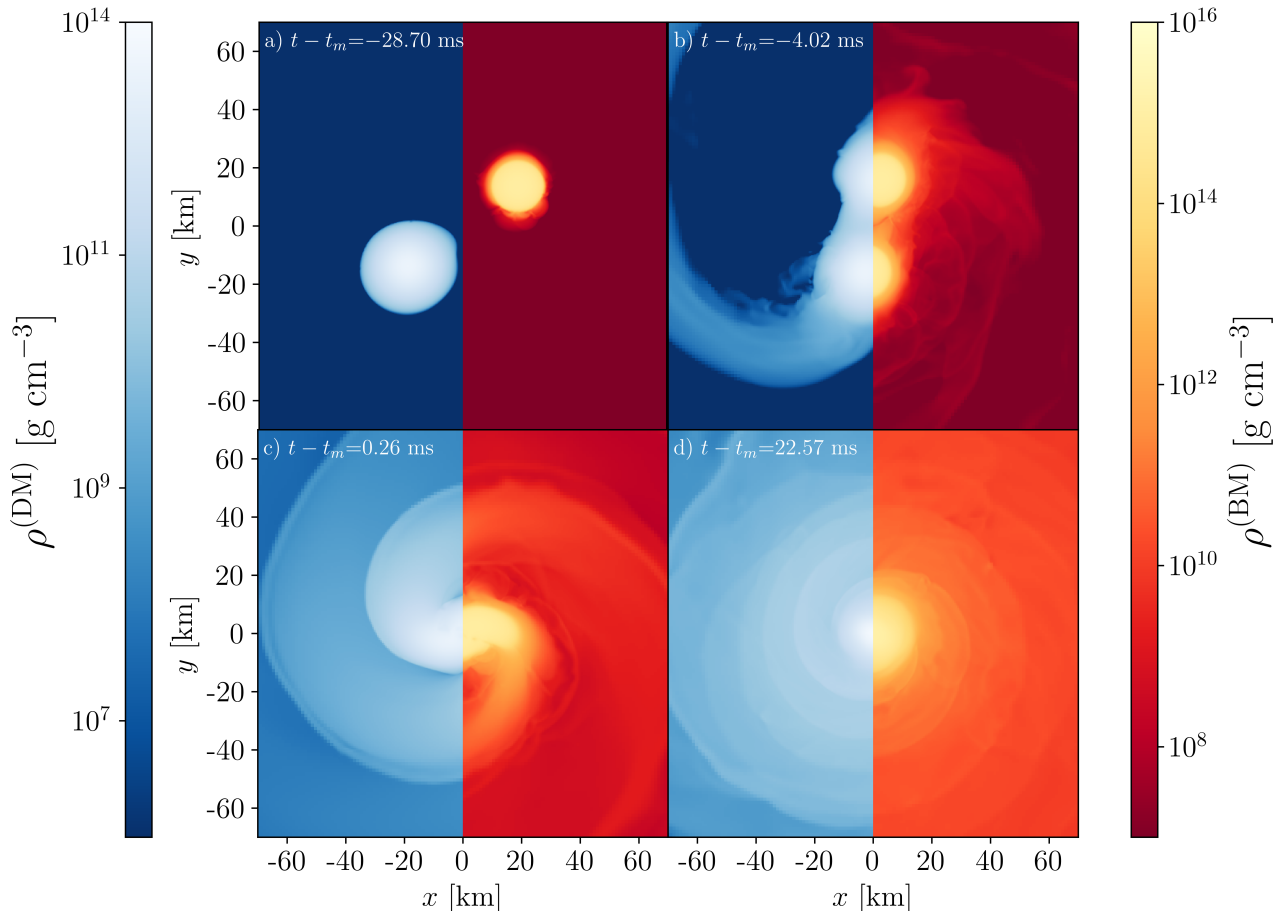


FIG. 2. Equatorial density distributions for both BM and DM components, for M24<sub>05H</sub><sup>R2</sup> run at selected times for  $M_{\text{tot}} = 2.4M_{\odot}$  with  $f_{\text{DM}} = 0.5\%$ . The presented times are  $t - t_m = (-28.7, -4.02, 0.26, 22.57)$  ms for the upper left, upper right, lower left, and lower right panel, respectively. Times  $c)$  and  $d)$  are the ones marked in Fig. 1 with the corresponding labels. The left halves (negative  $x$ ) show the DM density, whereas the right halves (positive  $x$ ) show the BM density.

each star is  $\rho_c^{(\text{BM})} = 7.837 \cdot 10^{14} \text{ g/cm}^3$ , while the initial central DM-halo density is  $\rho_c^{(\text{DM})} = 3.910 \cdot 10^{12} \text{ g/cm}^3$ , i. e., two orders of magnitude smaller. As the system evolves, tidal forces become more dominant. While BM just begins to show signs of deformation, the DM halos also respond to the gravitational influence of the companion star, developing a DM bridge with  $\rho^{(\text{DM})} \sim 10^9 \text{ g/cm}^3$

between the two stellar structures. At  $t - t_m = -4.02$  ms, panel  $b)$  of Figure 2, the DM components of the two NSs have already begun to merge, forming a common DM envelope that embeds both baryonic cores. This common DM envelope has implications for the subsequent evolution of the system, affecting the dynamics of the merger of the BM component and the properties of the final remnant. The BM distributions are also highly de-

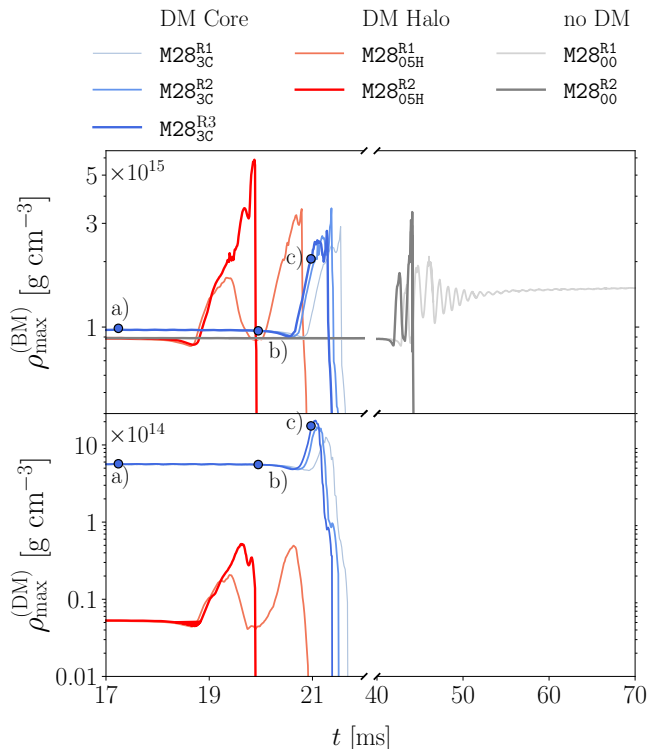


FIG. 3. Comparison of the central rest-mass densities during the merger and post-merger phase for BM (upper panel) and DM (lower panel) for the  $2.8M_{\odot}$  simulations. The central rest-mass density is extracted from the finest refinement level in each run. The points labeled with letters indicate the specific times that correspond to the 2D panels shown in Fig. 4. Due to a significant decrease in the rest-mass density after the collapse to a BH, the central rest-mass density of the fourth panel of Fig. 4, i. e., point  $d$ ), lies beyond the plotted range.

formed, with a clear indication of a developing BM bridge connecting the two stars at densities around  $10^{10} \text{ g/cm}^3$ . The post-merger snapshot at  $t - t_m = +22.57 \text{ ms}$  reveals the formation of a complex remnant, which can be seen in panel  $d$ ) of Figure 2. The BM has already merged into a central core with a maximum BM density of  $\rho_{\text{max}}^{(\text{BM})} = 1.138 \cdot 10^{15} \text{ g/cm}^3$ , surrounded by a more diffuse DM component, with a maximum DM density of  $\rho_{\text{max}}^{(\text{DM})} = 7.117 \cdot 10^{12} \text{ g/cm}^3$ . However, unlike the DM-core scenario, the DM distribution still shows an extended halo-like morphology, albeit with a higher central density.

Figure 3 shows the evolution of the central rest-mass density of BM and DM for the M28 simulations presented here. During the inspiral, these runs show similar behavior as in the previously discussed setup. Before the merger, we observed minor density oscillations in both fluids. During the merger, DM-halo simulations show a higher peak of the BM density compared to the DM-core or purely baryonic runs, suggesting that a diffuse halo may have an impact on the densities reached during

the merger. Furthermore, at low resolution R1, the  $M28_{00}^{\text{R1}}$  simulation produced an HMNS remnant, while the  $M28_{05\text{H}}^{\text{R1}}$  simulation exhibited a large bounce before collapsing to a BH. On the other hand,  $M28_{3\text{C}}^{\text{R1}}$  showed a direct increase in density, collapsing to a BH without any bounce. However, it is worth noting that the DM-free simulation had a longer inspiral due to the greater initial separation between the NSs. This longer inspiral could have led to increased numerical diffusion, potentially resulting in mass loss and preventing the immediate collapse to a BH. At mid-resolution,  $M28_{00}^{\text{R2}}$  exhibited a BM bounce followed by a collapse to BH. The  $M28_{05\text{H}}^{\text{R2}}$  do not show a bounce, but a gradual increase in the density of BM followed by a collapse to a BH. To further examine the dynamics and better visualize the merger, similar to the M24 case, we select four key time points ( $a$ ,  $b$ ,  $c$ ,  $d$ ) in Figure 3 that correspond to the 2D panels shown in Figure 4. These points represent different stages of the merger:  $a$ ) early inspiral,  $b$ ) formation of a BM/DM bridge linking the two stars,  $c$ ) merger time, and  $d$ ) post-merger phase, showing either the newly formed star or a BH.

Figure 4 shows the spatial distribution of the rest-mass density for both BM ( $\rho^{(\text{BM})}$ ) and DM ( $\rho^{(\text{DM})}$ ) in the  $M28_{3\text{C}}^{\text{R3}}$  run, where each baryonic star fully contains a dense DM core. The time evolution of this system is shown for four different snapshots, each labeled with the time relative to the merger time ( $t_m$ ). At  $t - t_m = -3.23 \text{ ms}$ , panel  $a$ ) shows the two DM-admixed NSs in the early stage of the inspiral, still relatively widely separated as they continue to orbit, with an initial central density of  $\rho_{\text{BM},c} = 9.729 \cdot 10^{14} \text{ g/cm}^3$  and  $\rho_{\text{DM},c} = 5.702 \cdot 10^{14} \text{ g/cm}^3$ . At  $t - t_m = -0.52 \text{ ms}$ , as the binary evolves, the stars undergo a significant tidal deformation in both fluids. While the DM remains in the inner regions of the baryonic star, the BM distribution begins to exhibit tidal perturbations due to their mutual gravitational interaction. A distinct BM bridge forms between the stars at densities around  $10^{10} \text{ g/cm}^3$ , indicating that the stars came into contact. On the other hand, the DM cores, even if tidally deformed, remain disconnected structures. This different behavior can be attributed to the significantly larger radius of the BM structure relative to the more compact DM core, resulting in the BM components merging prior to the DM cores. The third snapshot captures the dynamic phase of the BNS merger at  $t - t_m = 0.50 \text{ ms}$ , panel  $c$ ) of Figure 4. The two DM cores have finally merged into a single, central highly dense structure with  $\rho_{\text{max}}^{(\text{DM})} = 1.735 \cdot 10^{15} \text{ g/cm}^3$ . Note, this DM density is almost an order of magnitude lower than the BM counterpart, i. e.,  $\rho_{\text{max}}^{(\text{BM})} = 7.989 \cdot 10^{15} \text{ g/cm}^3$ , indicating that the BM remains the dominant component even in this phase of the merger. The final snapshot ( $t - t_m = 1.20 \text{ ms}$ , panel  $d$ ) shows the post-merger BH, identified by the green curve representing its apparent horizon. Notably, both fluids exhibit a prominent accretion disk structure, whose morphology indicates a significant angular momentum in the remnant.

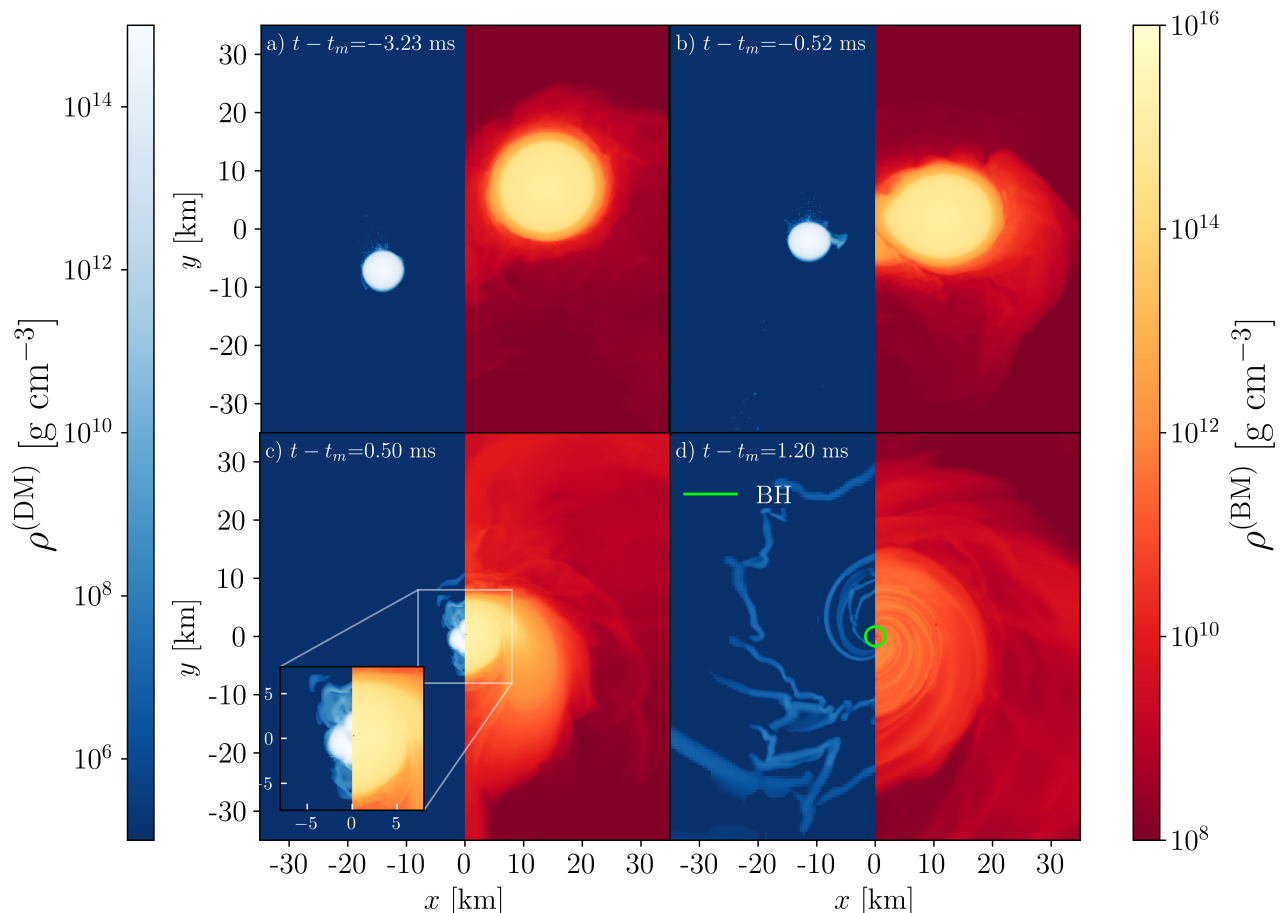


FIG. 4. Equatorial density distributions for both BM and DM components, for M28<sub>3C</sub><sup>R3</sup> run at selected times for  $M_{\text{tot}} = 2.8M_{\odot}$  with  $f_{\text{DM}} = 3\%$ . The presented times are  $t - t_m = (-3.23, -0.52, 0.50, 1.20)$  ms for the upper left, upper right, lower left, and lower right panel, respectively. Those times are the ones marked in Fig. 3 with the corresponding labels *a*), *b*), *c*) and *d*). The left halves (negative  $x$ ) show the DM density, whereas the right halves (positive  $x$ ) show the BM density.

### C. Remnant properties

Table II presents a summary of the merger outcomes for all simulated configurations.

We define a prompt collapse as the formation of a BH within the first 2 ms from the merger time. For the M28 configurations, a prompt collapse to a BH was observed, except for M28<sub>00</sub><sup>R1</sup>, which ends up as an HMNS. This discrepancy is attributed to the low resolution of the run. For M28<sub>00</sub><sup>R2</sup>, the full nucleonic run, the BH mass is  $2.484M_{\odot}$ . While in the case of a DM core configuration, i. e., M28<sub>3C</sub>, the BH masses are  $2.519M_{\odot}$  for R1,  $2.537M_{\odot}$  for R2 and  $2.539M_{\odot}$  for R3, for DM halos, i. e., M28<sub>05H</sub>, we obtained BH mass of  $2.403M_{\odot}$  for R1 and  $2.431M_{\odot}$  for R2. Notably, we observe that the BH mass tends to be greater when DM is concentrated in a dense core, compared to both DM-free runs and configurations with diluted halos. These results indicate a potential correlation between the DM morphology and the resulting BH mass. We note that the BH in DM-free simulations may have a lower mass due to mass diffusion related to the

longer inspiral. Regardless of this, the higher BH mass in DM-core configurations can be explained by the fact that the NSs are more compact and more tightly bound and therefore eject less mass during the merger. Moreover, the simulations indicate a possible effect of the DM morphology on the BH spin. M28<sub>3C</sub><sup>R2</sup> simulation shows a value of  $\chi = 0.537$  for DM cores. For the DM-free run M28<sub>00</sub><sup>R2</sup>, the resulting BH spin was  $\chi = 0.557$ . Simulations with DM halos, i. e., M28<sub>05H</sub><sup>R2</sup>, yielded a spin value of  $\chi = 0.541$ . These findings support the potential correlation between the DM configurations and the resulting BH mass and spin.

On the other hand, in  $2.4M_{\odot}$  configurations, HMNSs are consistently formed for all resolutions. In such remnants, a marginal increase in the maximum BM density of the HMNS was observed in simulations with a DM core, i. e., M24<sub>3C</sub>, compared to pure BM simulations and those with DM halos. These HMNSs exhibit an enhanced maximum density in the inner regions, resulting in denser post-merger environments. Specifically, at  $t - t_m = 25$  ms, the maximum BM densities are

$1.179 \cdot 10^{15}$ ,  $1.152 \cdot 10^{15}$  and  $1.151 \cdot 10^{15}$   $\text{g}/\text{cm}^3$  for  $\text{M24}_{3\text{C}}^{\text{R2}}$ ,  $\text{M24}_{00}^{\text{R2}}$  and  $\text{M24}_{05\text{H}}^{\text{R2}}$ , respectively. As anticipated, the DM core configurations show higher DM densities, reflecting their initial denser configuration.

We now turn to the overall post-merger matter distribution. DM-halo simulations  $\text{M24}_{05\text{H}}^{\text{R2}}$  show that in the post-merger the DM is distributed throughout the computational domain, maintaining a smooth halo-like structure. The same behavior of preserving the initial DM morphology is also present for DM cores. In fact, when initially considered concentrated in a core, DM tends to remain spatially constrained in the central region of the remnant. Notably, at  $t \lesssim 3$  ms after the merger, the DM density distribution exhibits a spatial offset between its center and the rotational center of the remnant. Specifically, the peak of the DM distribution is located approximately 2.49 km from the assumed rotational center with  $\rho_{\text{max}}^{(\text{DM})} = 2.493 \cdot 10^{14}$   $\text{g}/\text{cm}^3$ . Here, the center of rotation is considered to be the minimum of the lapse function in the computational domain and will be further discussed in Sec. III D. Later on in the merger, the  $\text{M24}_{3\text{C}}^{\text{R3}}$  remnant gradually undergoes a relaxation, resulting in a DM morphology closer to the ID. DM remains concentrated in the central region of the remnant, forming a core with a radius of  $\sim 6.3$  km, surrounded by a region of low DM density.

#### D. Angular-velocity evolution

To better understand the dynamic interplay between the two fluids, we analyzed the HMNS remnants considering angular velocity profiles. We first define the angular velocity  $\Omega^{(s)}$  as

$$\Omega \equiv \frac{d\phi}{dt} = \frac{dx^\phi}{dt} = \frac{u^\phi}{u^t}, \quad (20)$$

where  $u^t, u^i$  are the components of the four-velocity vector  $u^\mu$ . The corresponding three-velocity, as measured by the same Eulerian observer, can be evaluated as

$$v^{(s)i} \equiv \frac{\gamma_\mu^i u^{(s)\mu}}{-n_\mu u^{(s)\mu}} = \frac{1}{\alpha} \left( \frac{u^{(s)i}}{u^{(s)t}} + \beta^i \right). \quad (21)$$

The angular velocity from Eq. (20) within the 3+1 formalism is thus given by

$$\Omega^{(s)} = \alpha v^{(s)\phi} - \beta^\phi, \quad (22)$$

where

$$v^{(s)\phi} = \frac{xv^{(s)y} - yv^{(s)x}}{x^2 + y^2 + z^2}, \quad (23)$$

$$\beta^\phi = \frac{x\beta^y - y\beta^x}{x^2 + y^2 + z^2}, \quad (24)$$

are the three-velocity and the shift vector components computed from the Cartesian grid with coordinates

$(x, y, z)$ . Eq. (22) can be seen as the lapse-corrected part of the  $\phi$ -component of the three-velocity minus a frame-dragging term provided by the  $\phi$ -component of the shift vector [98]. We then define the azimuthally-averaged angular velocity  $\bar{\Omega}^{(s)}$  as

$$\bar{\Omega}^{(s)}(r, t) = \int_{-\pi}^{\pi} \Omega^{(s)}(r, \phi, t) d\phi. \quad (25)$$

A significant aspect of this analysis is the uncertainty in determining the precise center of rotation for each fluid component within the simulations. Due to the distinct distributions of the BM and DM components, the precise center of rotation is inherently uncertain and might not coincide for both fluid components. To address this, the minimum of the lapse function  $\alpha(x, y, z)$  within the simulation is used as the coordinate center, recognizing that it might not perfectly represent the rotational center of each component. To account for potential variations in the true rotational center relative to this coordinate center, we introduce a parameter  $\Delta^{(s)}$ , which represents the distance between the chosen center and the location of the lapse minimum. We generate a uniform distribution of 500 centers, where each point's  $\Delta^{(s)}$  range from 0 to a maximum of  $r_{\text{max}} = 0.5$  km. These points are drawn within a radius  $r_{\text{max}}$  around the minimum of the lapse function. For each of these 500 points, we then generate the associated  $\bar{\Omega}^{(s)}$  profiles. Given that these DM-admixed NS are predominantly composed of BM, the minimum of the lapse function is expected to track the BM rotational center more closely, leading to lower expected uncertainty in the BM profiles compared to the DM ones.

Figure 5 presents the radial profiles of the averaged fluid angular velocity,  $\bar{\Omega}^{(s)}(r, t)$ , on the equatorial plane for  $\text{M24}^{\text{R2}}$  runs, those with an HMNS remnant, without a BH collapse observed within the simulation time, at three different times after the merger  $t - t_{\text{m}} = 3, 6$  and 9 ms.

At  $t - t_{\text{m}} = 3$  ms, we observe quantifiable differences in the angular velocity profiles. At such early times after the merger, as the angular momentum is redistributed outward, the angular velocity profiles of both fluids exhibit significant variations, mainly in the closest-to-the-center regions. This angular momentum redistribution tends to reduce the central angular velocity of each fluid, creating different rotational zones within the stellar structure. In simulations with a diffuse DM halo, i.e.  $\text{M24}_{05\text{H}}^{\text{R2}}$ , the DM component shows a smoother angular velocity gradient, with a rotational frequency peaking [0.92 – 2.39] kHz, depending on the considered spatial offset  $\Delta^{(\text{DM})}$ . On the other hand, the DM core configuration shows a rapidly rotating DM sub-structure immediately after the merger. The DM rotational frequencies significantly exceed their BM counterpart, being  $\bar{\Omega}^{(\text{DM})} \in [2.05, 4.73]$ . The BM angular velocity profiles for DM-core and the DM-free runs show slight differences at small radii, exhibiting lower central angular velocities, i.e.,  $\bar{\Omega}^{(\text{BM})} \simeq 0.498$  kHz, compared to the other setups with HMNSs,  $\bar{\Omega}^{(\text{BM})} \simeq 0.967$

ID	Remnant	$M_{\text{BH}} [M_{\odot}]$	$\chi_{\text{BH}}$	$M_{\text{ejecta}}^{(\text{BM})} [M_{\odot}]$	$M_{\text{ejecta}}^{(\text{DM})} [M_{\odot}]$	$\rho_{\text{max}}^{(\text{BM})} [\text{gcm}^{-3}]$	$\rho_{\text{max}}^{(\text{DM})} [\text{gcm}^{-3}]$	$t_{\text{m}} [\text{ms}]$
M24 <sub>00</sub> <sup>R1*</sup>	HMNS	-	-	$1.76 \cdot 10^{-2}$	-	$9.95 \cdot 10^{14}$	-	57.09
M24 <sub>00</sub> <sup>R2*</sup>	HMNS	-	-	$4.27 \cdot 10^{-3}$	-	$1.15 \cdot 10^{15}$	-	53.65
M24 <sub>3C</sub> <sup>R1</sup>	HMNS	-	-	$1.24 \cdot 10^{-2}$	$2.12 \cdot 10^{-5}$	$1.14 \cdot 10^{15}$	$7.20 \cdot 10^{14}$	32.47
M24 <sub>3C</sub> <sup>R2</sup>	HMNS	-	-	$6.64 \cdot 10^{-3}$	$5.01 \cdot 10^{-6}$	$1.18 \cdot 10^{15}$	$7.88 \cdot 10^{14}$	30.92
M24 <sub>3C</sub> <sup>R3</sup>	HMNS	-	-	$5.13 \cdot 10^{-3}$	$1.41 \cdot 10^{-6}$	$1.25 \cdot 10^{15}$	$7.89 \cdot 10^{14}$	30.94
M24 <sub>05H</sub> <sup>R1</sup>	HMNS	-	-	$3.33 \cdot 10^{-3}$	$5.70 \cdot 10^{-5}$	$1.13 \cdot 10^{15}$	$6.59 \cdot 10^{12}$	30.42
M24 <sub>05H</sub> <sup>R2</sup>	HMNS	-	-	$2.99 \cdot 10^{-3}$	$4.95 \cdot 10^{-5}$	$1.15 \cdot 10^{15}$	$7.20 \cdot 10^{12}$	30.78
M28 <sub>00</sub> <sup>R1*</sup>	HMNS	-	-	$2.28 \cdot 10^{-2}$	-	$1.54 \cdot 10^{15}$	-	44.29
M28 <sub>00</sub> <sup>R2*</sup>	BH	2.484	0.557	$4.62 \cdot 10^{-3}$	-	$1.28 \cdot 10^{11}$	-	43.43
M28 <sub>3C</sub> <sup>R1</sup>	BH	2.519	0.530	$1.52 \cdot 10^{-3}$	0	$3.53 \cdot 10^{10}$	$5.68 \cdot 10^3$	22.32
M28 <sub>3C</sub> <sup>R2</sup>	BH	2.537	0.537	$2.06 \cdot 10^{-4}$	0	$1.10 \cdot 10^{10}$	$5.70 \cdot 10^3$	22.15
M28 <sub>3C</sub> <sup>R3</sup>	BH	2.539	0.538	$1.76 \cdot 10^{-5}$	0	$2.65 \cdot 10^9$	$5.71 \cdot 10^3$	22.08
M28 <sub>05H</sub> <sup>R1</sup>	BH	2.403	0.495	$3.89 \cdot 10^{-3}$	$3.57 \cdot 10^{-4}$	$2.86 \cdot 10^9$	$1.04 \cdot 10^{10}$	20.15
M28 <sub>05H</sub> <sup>R2</sup>	BH	2.431	0.541	$1.59 \cdot 10^{-3}$	$2.51 \cdot 10^{-6}$	$2.38 \cdot 10^8$	$2.38 \cdot 10^8$	20.23

TABLE II. Table of the presented simulations results at  $t - t_{\text{m}} = 25$  ms. The table lists simulation identifiers, remnant fate, BH mass  $M_{\text{BH}}$  and spin  $\chi_{\text{BH}}$ , BM and DM ejecta masses  $M_{\text{ejecta}}^{(\text{BM})}$  and  $M_{\text{ejecta}}^{(\text{DM})}$  (extracted at 295 km on the finest grid level present at such distance), maximum BM and DM densities  $\rho_{\text{max}}^{(\text{BM})}$  and  $\rho_{\text{max}}^{(\text{DM})}$ , evaluated from the finest grid level of the simulation, and merger time  $t_{\text{m}}$ . Starred identifiers, e. g. M24<sub>00</sub><sup>R1\*</sup>, have a larger initial separation distance, resulting in an offset for the merger times.

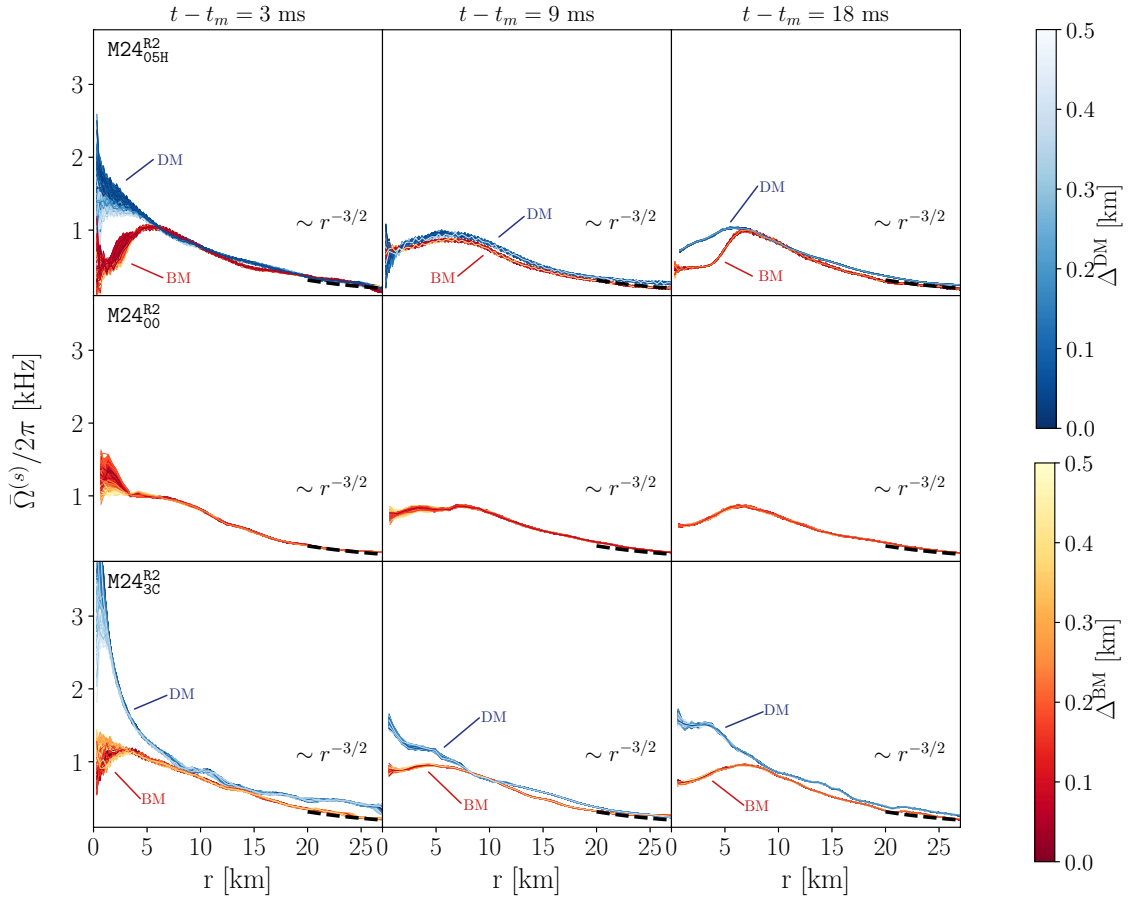


FIG. 5. Azimuthally-averaged angular velocity  $\bar{\Omega}^{(s)}(r, t)$  profiles on the equatorial plane for the M24<sup>R2</sup> simulations on the finest grid level. The parameter  $\Delta^{(s)}$  represents the distance between a chosen rotational center and the lapse-informed coordinate center. Dashed black lines serve as a reference profile scaling like  $\sim r^{-3/2}$ .

kHz and 1.285 kHz for  $M24_{3C}^{R2}$  and  $M24_{00}^{R2}$ , respectively.

As time evolves, at  $t - t_m = 9$  ms, the central DM angular velocity exhibits significant damping due to redistribution of the angular momentum. In DM-admixed HMNSs, we observed a substantial reduction in the central DM angular velocity  $\bar{\Omega}^{(DM)}$ . Notably, in the  $M24_{05H}^{R2}$  simulation, both DM and BM match closely throughout the remnant lifetime, showing similar profiles. However, the DM component maintains a slightly higher rotational frequency, with values of 0.873 kHz and 0.966 kHz for DM and BM, respectively. Nevertheless, DM cores still exhibit rapid rotation in the inner stellar regions. As evident in Fig. 5, the dense DM core still rotates considerably faster than the BM fluid, showing a higher angular velocity even when compared to the halo setup, with profiles even peaking at different radii, as shown in Table III.

At later times,  $t - t_m = 18$  ms, BM and DM distributions move towards a more stable equilibrium. In the  $M24_{05H}^{R2}$  simulation, the DM profile shows slight variations after the previously considered time steps. However, these profiles reveal a more complex rotational structure within the  $M24_{3C}^{R2}$  simulation. The DM core displays two distinct rotational regimes. The central region has a near-rigid rotation with an almost constant frequency. Beyond the DM core boundary, a gradual decrease in  $\bar{\Omega}^{(s)}$  is observed at larger radii. Without DM, the BM profiles of  $M24_{00}^{R2}$ , the BM profiles appear to approach a stable state. The remnant shows a deceleration along with a minor inward shift of the angular velocity peak. A qualitative comparison between  $M24_{3C}^{R2}$  and  $M24_{00}^{R2}$  indicates similarities in their profiles and behavior. However, BM profiles of  $M24_{05H}^{R2}$  exhibit a central plateau. In the inner stellar regions, the fluid maintains a relatively uniform angular velocity  $\bar{\Omega}^{(BM)} = 0.48$  kHz up to a radius of  $\sim 3.9$  km, followed by a marked increase that reaches its peak  $\bar{\Omega}^{(BM)} = 1.002$  kHz at  $\sim 6.7$  km, remarkably similar to the DM one  $\bar{\Omega}^{(BM)} = 1.026$  kHz at  $\sim 5.5$  km. All configurations show the expected behavior at asymptotically large radii, decreasing monotonically as  $\propto r^{-3/2}$  [98], see black dashed line in Fig. 5.

### E. Ejecta Masses

In this work, the ejecta properties are determined by computing them on a series of concentric extraction spheres, with radii ranging between 295 km and 1030 km. On each spherical surface, we computed the integrated fluxes of mass, energy, and momentum for outgoing unbound matter. The matter is considered unbound on these extraction surfaces if it satisfies the geodesic criterion [99]:

$$u_t < -1 \text{ and } v_r > 0, \quad (26)$$

where  $u_t$  and  $v_r$  are, respectively, the time component of the fluid four-velocity and the radial velocity. Figures 6 and 7 present the evolution of the ejecta mass for M24 and M28, respectively.

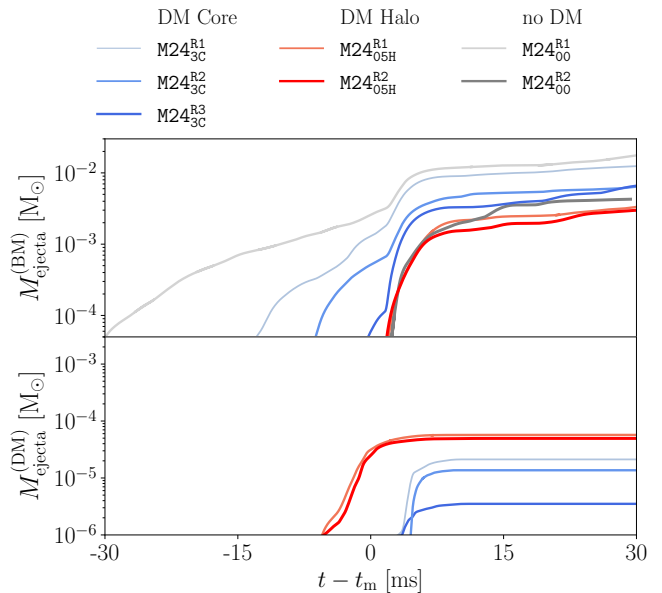


FIG. 6. The ejecta mass as a function of time for the M24 BNS runs. The upper panels show the BM ejecta ( $M_{\text{BM,ejecta}}$ ), while the lower panels present the DM ejecta ( $M_{\text{DM,ejecta}}$ ). All ejecta curves shown here are extracted at the smallest extraction radius, i. e.,  $r = 295$  km, on the finest level available.

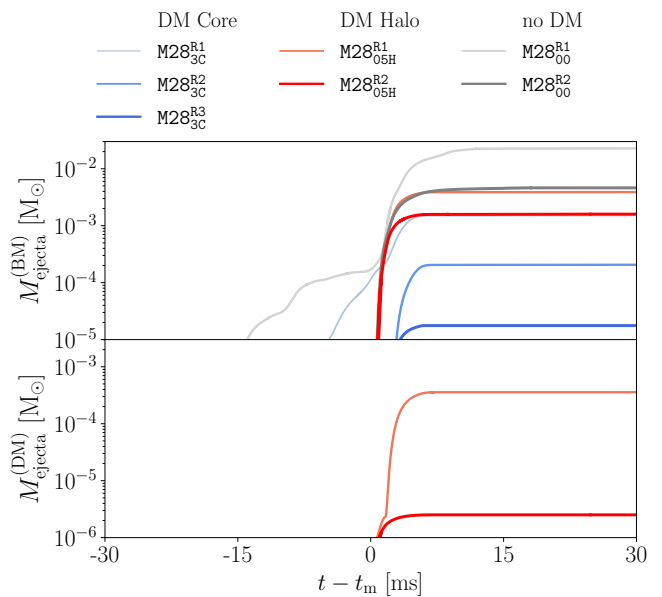


FIG. 7. The ejecta mass as a function of time for the M28 BNS runs. The upper panels show the BM ejecta ( $M_{\text{BM,ejecta}}$ ), while the lower panels present the DM ejecta ( $M_{\text{DM,ejecta}}$ ). All ejecta curves shown here are extracted at the smallest extraction radius, i. e.,  $r = 295$  km, on the finest level available.

ID	$t - t_m$ [ms]	$\bar{\Omega}_{\max}^{(\text{BM})}$ [kHz]	$\bar{\Omega}_{\max}^{(\text{DM})}$ [kHz]	$r_{\bar{\Omega}_{\max}^{(\text{BM})}}$ [km]	$r_{\bar{\Omega}_{\max}^{(\text{DM})}}$ [km]
M24 <sub>00</sub> <sup>R2</sup>	3	1.285	-	1.106	-
	9	0.871	-	6.991	-
	18	0.854	-	6.461	-
M24 <sub>05H</sub> <sup>R2</sup>	3	1.062	1.736	5.376	0.436
	9	0.873	0.966	5.257	5.876
	18	1.002	1.026	6.762	5.460
M24 <sub>3C</sub> <sup>R2</sup>	3	1.153	3.961	2.238	0.350
	9	0.967	1.629	2.896	0.479
	18	0.954	1.578	6.70	0.522

TABLE III. Table of maximum angular velocities  $\bar{\Omega}_{\max}^{(s)}$  in kHz and their corresponding radial distances  $r_{\bar{\Omega}_{\max}^{(s)}}$  in km for both BM and DM at different times  $t - t_m$  in milliseconds. The  $\bar{\Omega}_{\max}^{(s)}$  values are averaged over all possible values of parameter  $\Delta^{(s)}$ .

### 1. BM ejecta

In the M28 configurations, the BM ejecta mass increases gradually with time for all setups, as expected. However, the ejecta mass reaches a stable plateau due to the suppression of the ejecta following the formation of a BH. The simulations without DM show a rapid increase in the ejecta mass, followed by those with a DM halo, with a lower plateau, indicating a slightly lower ejecta mass. On the other hand, simulations with DM cores exhibit significantly different behavior, with the M28<sub>3C</sub> ejecta being suppressed by  $\sim 2$  orders of magnitude. This suggests that in higher mass systems, a dense DM core can actively suppress the ejection of BM. For the M24 configurations, the general expectation would be a decreased BM ejecta mass in scenarios with a DM core, due to the DM-enhanced gravitational field, potentially suppressing the ejection [40]. However, our simulations, e.g. M24<sub>3C</sub>, show a significantly more violent merger, characterized by shock-driven ejecta. Moreover, compared to the DM-free run, this configuration displays a more pronounced bounce during the merger. This causes extra shock-driven ejecta and a larger bounce, leading to more BM ejecta. On the other hand, DM-halo configurations, while affecting the merger itself, do not seem to change the BM ejecta mass significantly compared to full BM setups. Our mid-resolution BM run, M24<sub>00</sub><sup>R2</sup>, exhibits a similar amount of ejecta, as shown in Table II. The consistent trends across different resolutions indicate that the results are robust and are not significantly altered by numerical artifacts.

### 2. DM ejecta

Beyond the BM ejecta, our simulations also reveal the presence of the DM ejecta, providing direct insight into its dynamic behavior during these mergers. In the M24 configurations, for DM halos, the ejecta mass of M24<sub>05H</sub><sup>R2</sup> reaches a plateau around  $5 \cdot 10^{-5} M_{\odot}$ . In comparison, DM cores show reduced ejecta masses, saturating at  $5 \cdot 10^{-6} M_{\odot}$  for M24<sub>3C</sub><sup>R2</sup>. This suggests that diluted configura-

tions lead to significantly greater DM ejecta compared to the dense DM core scenario.

In the M28 configurations, the DM ejecta mass shows a similar trend. While the DM halos show a rapid increase of ejecta mass, reaching a plateau around  $3 \cdot 10^{-6} M_{\odot}$  for M28<sub>05H</sub><sup>R2</sup> the DM core simulations show a complete absence of DM ejecta. This behavior demonstrates that prompt collapse in such massive systems, when coupled with a dense DM core, results in the complete capture of DM by the forming BH, effectively halting the ejection.

## F. Gravitational Waves

In this section, we extract the GW signals from the simulations at different extraction radii  $r_{\text{ext}}$ , using the retarded time coordinate

$$u = t - r_{\text{ext}} - 2M \ln \left[ \frac{r_{\text{ext}}}{2M} - 1 \right], \quad (27)$$

where  $t$  is the simulation time. We show the results of the extracted GWs in terms of the dominant  $(2, |2|)$ -mode strain for different DM configurations and resolutions at a fixed  $r_{\text{ext}}$  in Fig. 8. The waveforms of different resolutions are then tested for convergence by comparing and scaling the phase difference between (R3-R2) and (R2-R1).

We then compare the GW signals (extracted at a common largest  $r_{\text{ext}}$  per configuration) resulting from the NR simulations with an existing GW model for BNS systems without DM. In this case, we use the IMRPhenomXAS\_NRTidalv3 model [100, 101] for the comparisons. This model employs the IMRPhenomXAS model for the dominant  $(2, |2|)$  mode GWs from aligned-spin binary black hole (BBH) systems [102]. On the other hand, NRTidalv3 is the latest version of the modular, phenomenological NRTidal series [103–105] that describes the tidal effects that are prevalent for BNS systems, which arise from the tidal interactions between the NSs.

For the comparison, we align the NR waveforms of different configurations with the corresponding IMRPhenomXAS\_NRTidalv3 waveform by computing the time and phase shifts  $\delta t$  and  $\delta \phi$  that minimize the fol-

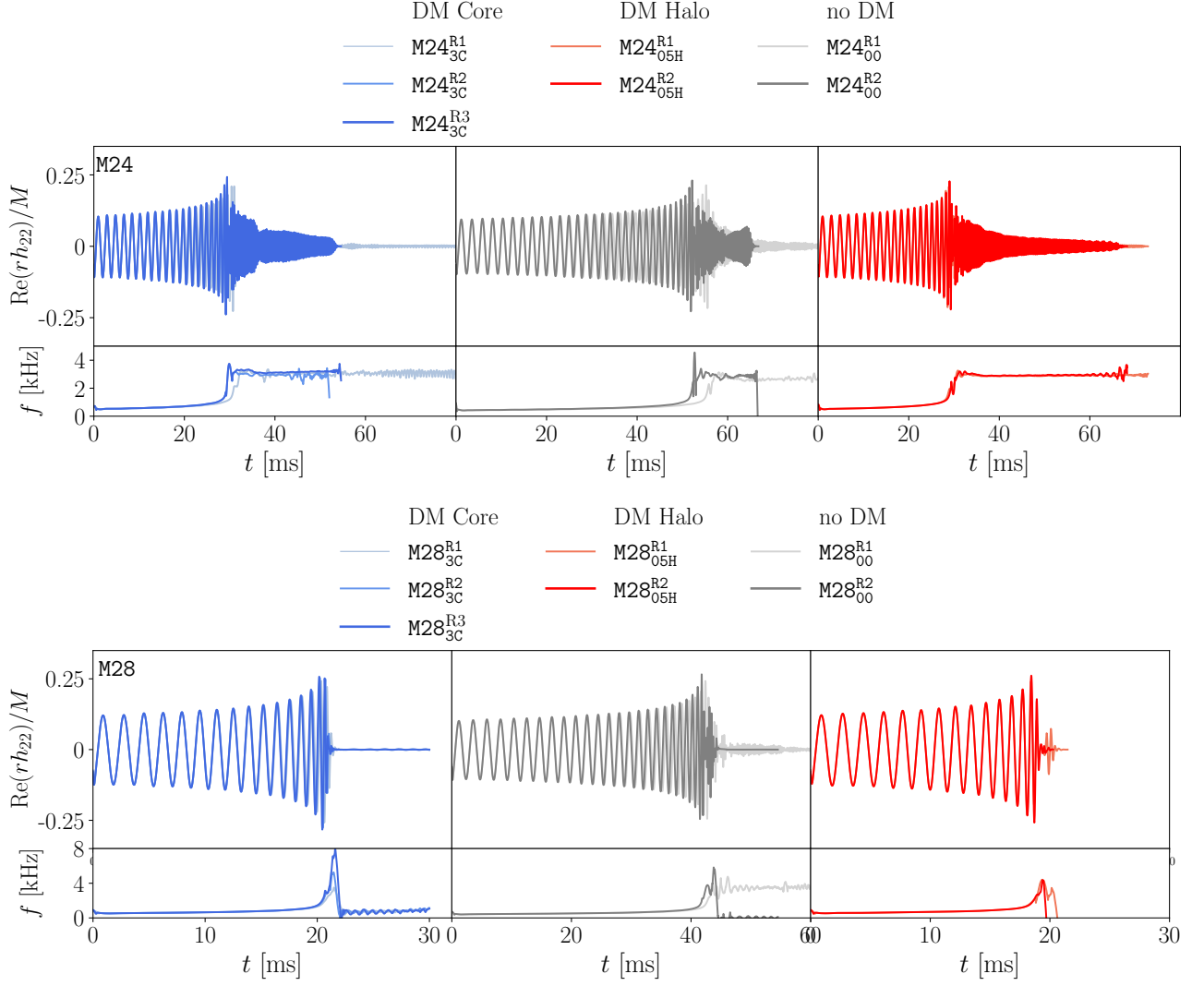


FIG. 8. Waveform strain and instantaneous frequency of the  $\ell = |m| = 2$  mode GW signal for all the simulations run. **Top panel:** shows simulations with total gravitational mass  $2.4 M_{\odot}$  for R1, R2 and R3. All the GW waveforms are extracted at  $r = 1474.21$  km. **Bottom panel:** Same as the top panel for simulations with total gravitational mass  $2.8 M_{\odot}$ .

lowing integral [106]:

$$\mathcal{I}(\delta t, \delta\phi) = \int_{t_1}^{t_2} dt |\phi_{\text{NR}}(t) - \phi_{\text{Model}}(t + \delta t) + \delta\phi|, \quad (28)$$

over some alignment window bounded by the time interval  $[t_1, t_2]$ , which is chosen near the beginning of the NR waveform.

We show the results of these comparisons in Fig. 9. For each NR simulation, we show in the figure the (2,2)-mode waveform strain of the highest resolution R3 and its phase difference with the model. The error band or uncertainty is calculated by taking the phase difference between the two highest resolutions of the NR simulations. For the configurations without DM and with a DM core, we observe relatively good agreement between the waveform and the model, whose

$\Lambda$  are similar up to  $\mathcal{O}(10)$  between the configurations. However, huge deviations (green) from the error bands are seen for the halo DM configuration, using the  $\Lambda^{\text{out}}$  that was computed under the assumption of a two-fluid treatment, where the DM and BM only interact gravitationally, and without proper consideration of the dilute and extended nature of the halo. If we assume the  $\Lambda$  to be similar to the other configurations up to ( $\mathcal{O}(10)$ ), i. e.  $\Lambda^{\text{est}} = [810, 340]$  for  $M = [2.4, 2.8]$  the phase difference (orange) is significantly reduced and the agreement between the waveform and the model improves. This implies a need for more accurate calculations of the tidal deformability for the two-fluid system in which one component is much more extended and dilute in comparison to the second one. Particularly, calculations for DM and BM interacting only gravitationally [29, 62, 97, 107, 108],

ID	$f_2^{\text{NR}}$ [kHz]	$f_2^{\text{fit}}(\Lambda^{\text{out}})$ [kHz]	$f_2^{\text{fit}}(\Lambda^{\text{est}})$ [kHz] [109]
M24 <sub>00</sub> <sup>R2</sup>	3.457	3.625	-
M24 <sub>3C</sub> <sup>R2</sup>	3.578	3.642	-
M24 <sub>3C</sub> <sup>R3</sup>	3.811	3.642	-
M24 <sub>05H</sub> <sup>R2</sup>	3.505	2.774	3.633

TABLE IV. The  $f_2$  frequencies of the M24 runs compared to the quasi-universal fit, evaluated using  $\Lambda^{\text{out}}$  and the estimated  $\Lambda^{\text{est}}$ .

and where the halo is extended, should be improved.

Figure 10 shows the spectral density of the GW signals as a function of the frequency. The M24<sup>R2</sup> signals, representing simulations with the same resolution R2, show consistent peak frequencies, suggesting robustness in the dominant mode,  $f_2^{\text{NR}} = 3.457, 3.505, 3.578$  kHz, for M24<sub>00</sub><sup>R2</sup>, M24<sub>05H</sub><sup>R2</sup>, M24<sub>3C</sub><sup>R2</sup>, respectively. Table IV presents the extracted frequencies and their comparison with quasi-universal relation predictions [109], as

$$M_{1.4}f_2 \text{ [kHz]} = \sum_{i=0}^5 g_i (\log_{10} \Lambda)^i, \quad (29)$$

where

$$g_i \in [4.2590, -0.47874, -0.45353, 0.14439, -0.016194, 0.00064163], \quad (30)$$

$M_{1.4}$  indicates the rescaling for a 1.4  $M_\odot$  NS, and  $\Lambda_f$  is the tidal deformability, evaluated using  $\Lambda^{\text{out}}$ .

Moreover, the M24<sub>3C</sub><sup>R3</sup> signal shows a noticeable shift towards higher frequencies, i.e.  $f_2^{\text{NR}} = 3.811$  kHz. This observed shift suggests a potential dependence on either the DM-core presence or a numerical effect arising from the increased resolution of the run. Disentangling these influences is crucial for an accurate interpretation of the results. Therefore, further runs are required. Specifically, higher-resolution simulations of the halo and DM-free configurations are essential to determine if the shift is a DM-core feature.

As shown in Table IV, the quasi-universal relation exhibits a 20% deviation when  $\Lambda^{\text{out}}$  is used to evaluate the frequency peak  $f_2$ . In contrast, employing  $\Lambda^{\text{est}}$  yields a frequency more consistent with that inferred from the NR simulation, with a deviation of  $\sim 3.65\%$ .

#### IV. CONCLUSIONS

This study presents, up to our knowledge, the first simulations of DM-admixed BNS systems within a full GR framework employing constraints-solved ID. Quasi-equilibrium configurations are generated using the updated SGRID code [41]. These IDs are constructed employing the SLy4 EOS for BM and modeling DM as a non-interacting Fermi gas. We investigate DM-admixed

BNSs with two distinct morphologies: a dense DM core fully embedded within the BM star and a diluted DM halo encompassing the entire BM structure. Simulations are performed for total system masses of  $2.4M_\odot$  and  $2.8M_\odot$  to better explore the impact of DM on merger dynamics and remnant fate in a broader parameter space. We establish a clear comparison by running DM-free simulations, allowing us to better isolate DM's effects from inherent NR uncertainties. In the following, we summarize our main findings:

- **Merger dynamics and DM structure:** The merger time of DM structures is highly sensitive to the spatial extent of the DM component. Extended DM halos come into contact earlier, forming a common envelope around the inspiraling BM stars. Contrary, the DM cores remain distinct and tidally deformed when the BM structures come into contact. Notably, the merger preserves the DM morphology of the ID. Simulations resulting in an HMNS from DM-core configurations retained a core-like DM structure in their central regions. On the other hand, DM-halo configurations evolve into a more diffuse and spatially extended cloud-like DM distribution surrounding the HMNS.
- **Remnant fate and mass dependence:** For lower mass systems, i.e. M24, simulations yield HMNS remnants. The presence of DM, particularly in core configurations, lead to increased central BM densities and more compact remnants, reflecting the initial conditions of the system where the enhanced gravitational pull of the dense DM core creates more tightly bound configurations, with greater central densities. On the other hand, higher mass systems, i.e., M28, experience a prompt collapse to a BH. In these cases, DM tends to shorten the remnant's lifespan, favoring gravitational instabilities and the formation of a BH. The final BH mass exhibits a weak dependence on the DM morphology, with DM-core simulations resulting in slightly higher BH masses compared to DM-free or DM-halo configurations. We emphasize that DM-free simulations may yield lower BH mass due to a longer binary inspiral, potentially leading to greater mass diffusion compared to the other setups.
- **Rotational dynamics:** Our analysis of the post-merger rotational evolution suggests potential differences in angular velocity based on DM morphology. DM cores exhibit higher rotational velocities compared to DM halo configurations. While BM angular velocity shows less pronounced changes, halo configurations show the presence of a central region with lower BM angular velocities, suggesting a more complex rotational profile.
- **BM ejecta masses:** Our simulations reveal the impact of DM morphology on both BM and DM ejecta: DM-core configurations can suppress BM

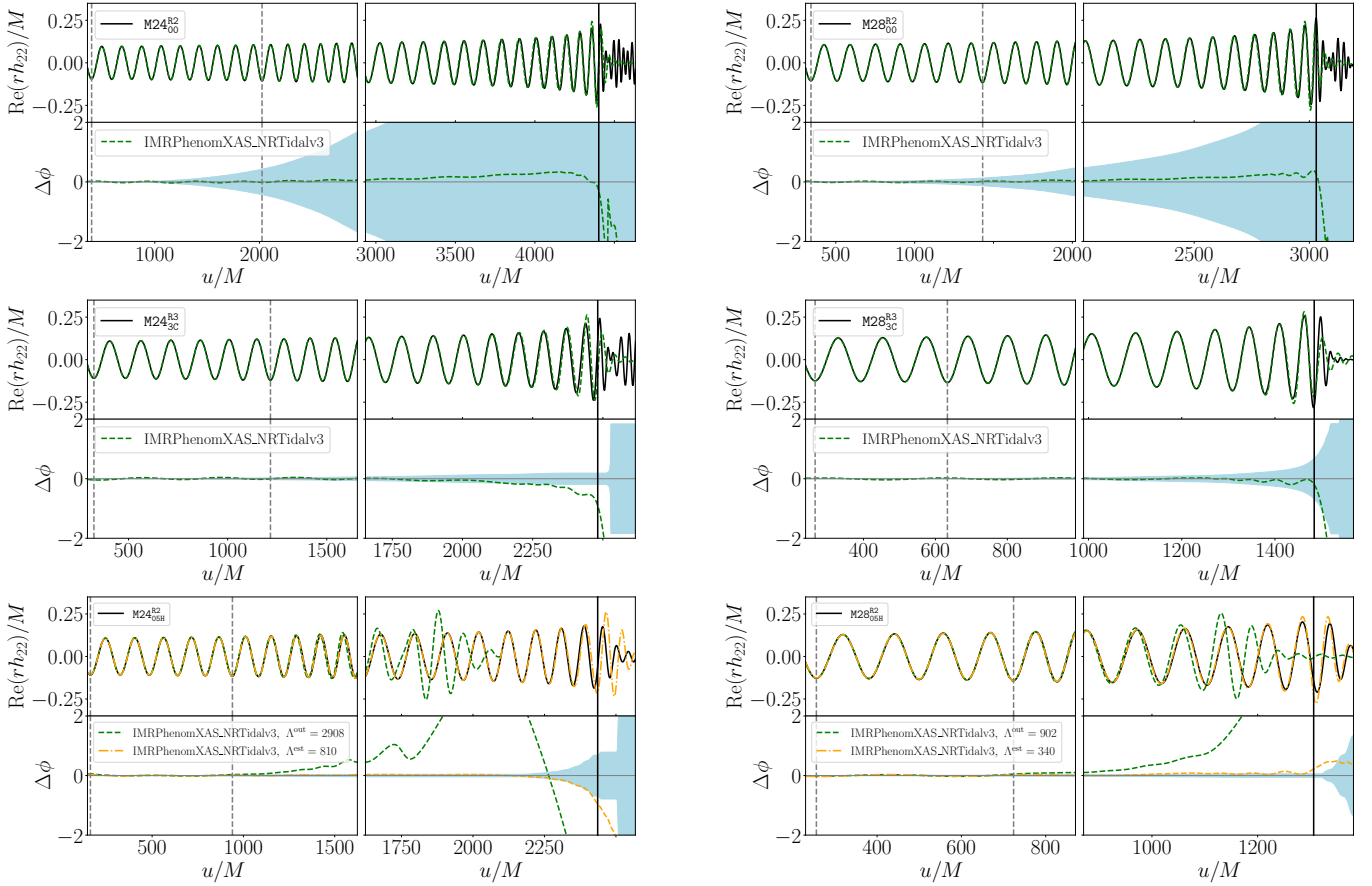


FIG. 9. Time-domain dephasing comparisons for the different NR configurations with the `IMRPhenomXAS_NRTidalv3` model. For each NR waveform, the upper panel shows the real part of the gravitational wave strain as a function of the retarded time, while the bottom panel shows the phase difference between the waveform model and the NR waveform, together with the light blue error bands. The alignment window is indicated by the gray dashed vertical lines in the early inspiral, while the merger is indicated by the solid black vertical line. For the halo configurations, we introduce a comparison with the same waveform approximant but this time with an estimated tidal deformability  $\Lambda^{\text{est}}$ , comparable to those of the other DM configurations. This results in a phase difference that is also comparable to the phase differences observed for the purely baryonic and the DM-core configurations. The bottom panels (for the DM-halo configurations) show the comparison between the two choices for the tidal deformability. Green lines represent the GW obtained when using a tidal deformability computed assuming that the star extends to the edge of the halo. Orange lines show the GW obtained when using an estimated  $\Lambda$  and agree better with the black NR waveform.

ejection in higher mass systems. At the same time, for less massive systems, DM-cores seem to enhance shock-driven BM ejecta via more violent mergers. On the other hand, DM halos generally lead to similar BM ejecta compared to the DM-free scenario. These trends are robust across different resolutions.

- **DM ejecta masses:** We observe DM ejecta in the range  $[10^{-6}, 10^{-4}]M_{\odot}$  in the presented mergers. These trends are robust across different resolutions; however, they are expected to be sensitive on the DM EOS and the temperature dependence of the DM. Furthermore, we expect that the component masses and the BM EOS also play a crucial role in determining the DM ejecta. While it is possible that these ejecta may form DM sub-structures and/or subsequently be accreted by other stellar

objects, this scenario requires confirmation through further research. Indeed, the ejected DM during the merger might be lately accreted by other objects in the vicinity, leading to *DM recycling*. Understanding the viability of this mechanism is of interest for refining models of DM accumulation in astrophysical objects.

- **GW signal and Tidal Deformability:** GW signal extraction from our simulations reveals a significant deviation in tidal deformability calculations for halo configurations when it is calculated in a two-fluid framework. Employing a tidal deformability value similar to that of the pure BM and DM core configurations significantly improves the agreement between the DM-halo configuration and the `IMRPhenomXAS_NRTidalv3` wave-

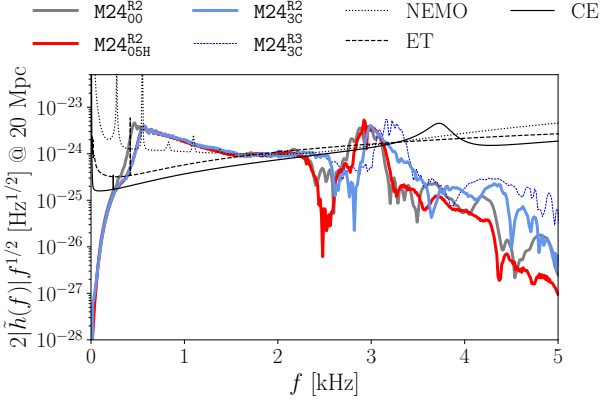


FIG. 10. Spectral density of the  $M24^{R2}$  GW signals as a function of frequency  $f$  [kHz]. The solid, dashed, and dotted black curves depict the sensitivity curves for Cosmic Explorer (CE), Einstein Telescope (ET), and NEMO respectively.

forms, highlighting the need for refined calculations for DM-admixed NSs. This initial finding indicates that regions of the  $f_\chi - m_\chi$  parameter space previously considered excluded by the GW data may need to be revisited. This could imply that extended DM halos may indeed be consistent with the GW170817 and GW 190425 binary NS mergers, contrary to conclusions drawn from previous results [88].

### ACKNOWLEDGMENTS

The authors thank William Newton for providing the SLy4 EOS tabulated to high-density, enabling the exploration of extreme density regimes reached in the simulations. The authors acknowledge Nils Andersson for his significant contributions through discussions and his help in interpreting the analysis. The work of E.G., H.R.R. and C.P. was supported by national funds from FCT – Fundação para a Ciência e a Tecnologia within the projects UIDP/04564/2020 and UIDB/04564/2020, respectively, with DOI identifiers 10.54499/UIDP/04564/2020 and 10.54499/UIDB/04564/2020. E.G. also acknowledges the support from Project No. PRT/BD/152267/2021. E.G. and V.S. acknowledge the support from FCT – Fundação para a Ciência e a Tecnologia within the project “Fundamental physics with neutron stars and their mergers” (Grant No. 2023.10526.CPCA.A2 with DOI identifier 10.54499/2023.10526.CPCA.A2). H.R.R. acknowledges financial support from the FCT – Fundação para a Ciência e a Tecnologia, I.P., within the Project No. EXPL/FIS-AST/0735/2021. H.R.R. acknowledges financial support provided under the European Union’s H2020 ERC Advanced Grant “Black holes: gravitational engines of discovery” grant agreement no. Gravitas-101052587. Furthermore, TD acknowledges fund-

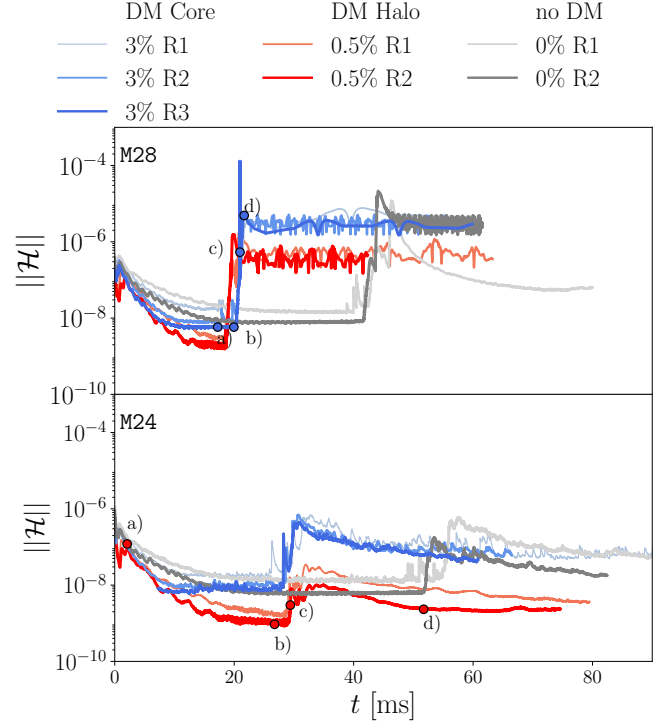


FIG. 11. Time evolution of the L2-norm of the Hamiltonian constraints on the second to finest level for the simulations setup. The top panel represents the system with the total gravitational mass of  $2.8 M_\odot$ , while the bottom panel corresponds to  $2.4 M_\odot$ .

ing from the EU Horizon under ERC Starting Grant, no. SMArt-101076369. Views and opinions expressed are however those of the authors only and do not necessarily reflect those of the European Union or the European Research Council. Neither the European Union nor the granting authority can be held responsible for them. V.S. gratefully acknowledges support from the UKRI-funded “The next-generation gravitational-wave observatory network” project (Grant No. ST/Y004248/1). W.T. was supported by NSF grants PHY2136036 and PHY-2408903. The authors gratefully acknowledge the Gauss Centre for Supercomputing e.V. for funding this project by providing computing time on the GCS Supercomputer SuperMUC-NG at Leibniz Supercomputing Centre [project pn29ba], the national supercomputer HPE Apollo Hawk at the High-Performance Computing (HPC) Center Stuttgart (HLRS) under the grant number GWanalysis/44189, and we acknowledge the usage of the DFG-funded research cluster jarvis at the University of Potsdam (INST 336/173-1; project number: 502227537).

### Appendix A: L2-norm of the Hamiltonian constraint

Figure 11 shows the evolution of the L2-norm of the Hamiltonian constraint for the simulations run within

this framework. All runs exhibit an initial burst of constraint violation within the first few milliseconds, followed by a rapid decrease related to the constraint damping of the Z4c formalism [80, 81]. Following this initial phase, the configurations evolve differently. For  $2.8 M_{\odot}$ , all runs, except for  $M28_{00}^{R1}$ , exhibit a sudden increase in the Hamiltonian constraint violation around  $t \sim 20$  ms. Figure 11 also shows that  $M28_{00}^{R3}$  has a spike in  $\|\mathcal{H}\|$  at  $t = 20.97$  ms. We note that such a feature is not observed at the lower resolutions. This spike is strongly related to the formation of a BH. The collapse of the NS to a BH is a highly dynamic process that generates a strong gravitational field and, consequently, a larger constraint violation. However, we note that  $M28_{00}^{R1}$  does not show such a collapse. The post-merger behavior follows the trend expected for a constraint damping formalism. On the other hand, the  $2.4M_{\odot}$  runs, regardless of the DM morphology, do not show a sharp increase in violation of the constraints due to the BH formation. Instead, they show a more 'controlled' evolution, although the different DM profiles affect the magnitude of the constraint violation.

### Appendix B: Rest Mass Evolution

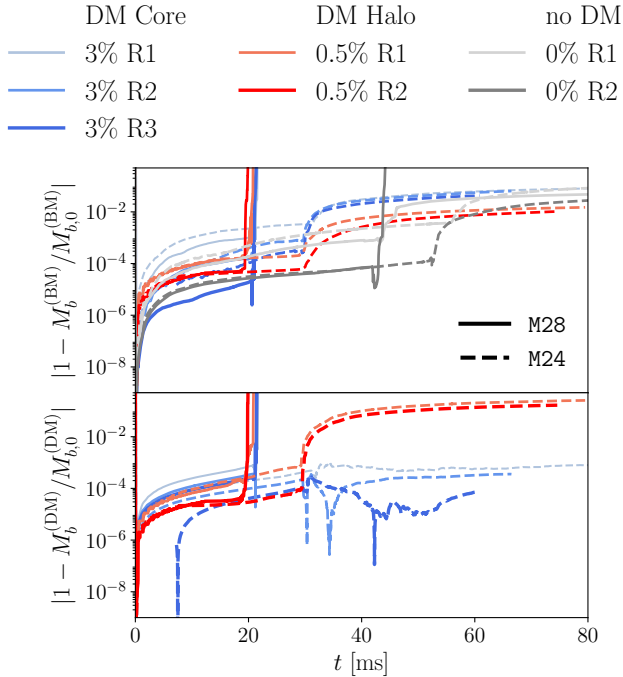


FIG. 12. Rest mass and its relative change as a function of time for BM (upper panels) and DM (lower panels). All the values are extracted at level  $l = 1$ .

The performance of the conservative adaptive mesh refinement can be tested by checking the rest mass conservation of the system. The rest mass in the simulations

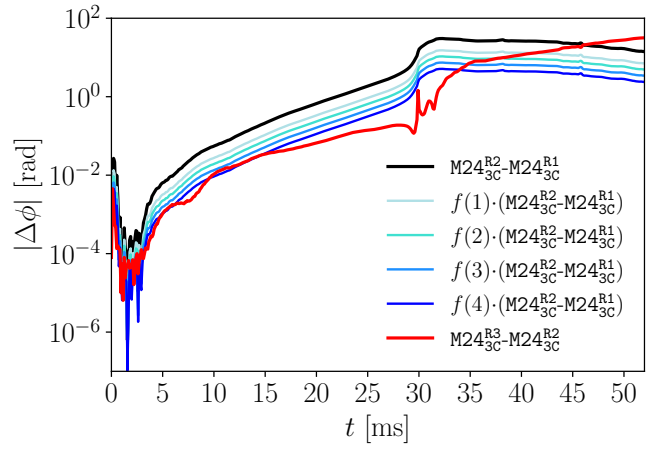


FIG. 13. Evolution of the absolute value of the phase difference between the waveforms at different resolutions,  $M24_{3C}^{R2} - M24_{3C}^{R1}$ ,  $M24_{3C}^{R3} - M24_{3C}^{R2}$ , and the rescaled phase difference assuming  $n$ -th order of convergence.

can be evaluated as

$$M_b^{(s)} = \int d^3x \sqrt{\gamma} D^{(s)}. \quad (\text{B1})$$

This quantity should remain constant during the whole evolution if mass losses (or sources) are not present in the simulation. The rest-mass in the BAM code is evaluated on each refinement level. Figure 12 shows the time evolution of the relative change in rest masses  $M_b^{(s)}$  evaluated at level 1 relative to the initial value  $M_{b,0}^{(s)}$ . The figure depicts that the rest masses of the fluid are consistently conserved during the merger, showing average relative changes of the order of  $\sim 10^{-5}$ , consistent with previous studies [71]. Lower resolution simulations yield larger variations, indicative of increased numerical errors. Simulations that result in BH formation display a sharp decrease in the rest mass, a known numerical artifact of the BAM code's handling of matter during BH formation. Moreover, for  $M24_{3C}$ ,  $M24_{00}^{R1}$ ,  $M28_{00}^{R1}$ , a noticeable decrease in BM rest-mass is observed as a significant fraction of ejecta reaches the refinement level boundary and exits the computational grid. The same behavior can be seen in  $M24_{05H}$  simulations for the DM rest-mass.

### Appendix C: GW Convergence

The scaling function used to determine the convergence order is defined as:

$$f(n) = \frac{\Delta x_{R3}^n - \Delta x_{R2}^n}{\Delta x_{R2}^n - \Delta x_{R1}^n} = \frac{N_{R3}^{-n} - N_{R2}^{-n}}{N_{R2}^{-n} - N_{R1}^{-n}}, \quad (\text{C1})$$

where  $\Delta x_{R3}^n$  and  $N_{R3}^n$  are the grid spacing and the number of points in one dimension in a specific resolution  $Ri$ , respectively, and  $n$  is the order of convergence.

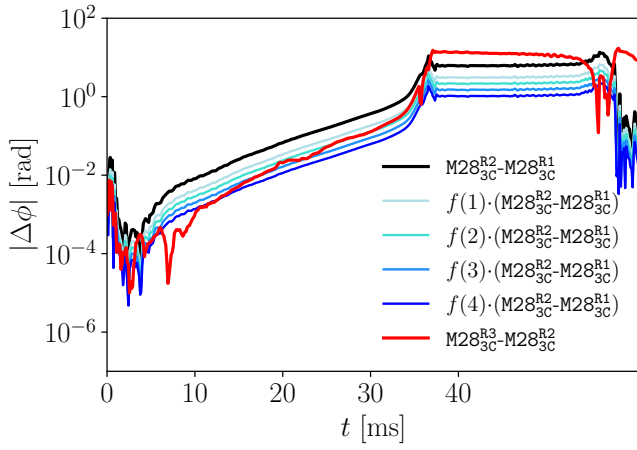


FIG. 14. Evolution of the absolute value of the phase difference between the waveforms at different resolutions,  $M28_{3c}^{R2}-M28_{3c}^{R1}$ ,  $M28_{3c}^{R3}-M28_{3c}^{R2}$ , and the rescaled phase difference assuming  $n$ -th order of convergence.

As shown in Figs. 13-14, there is no clear convergence order that scales the phase difference between the resolutions reasonably during the whole inspiral. Regardless of this, the phase difference decreases with increasing resolution in a monotonic and consistent manner. Given the lack of convergence order, we adopt the difference between the highest resolution as an error estimate in Figs. 9.

- 
- [1] B. P. Abbott *et al.* (LIGO Scientific, Virgo), GW170817: Observation of Gravitational Waves from a Binary Neutron Star Inspiral, *Phys. Rev. Lett.* **119**, 161101 (2017), [arXiv:1710.05832 \[gr-qc\]](#).
  - [2] B. P. Abbott *et al.* (LIGO Scientific, Virgo), Estimating the Contribution of Dynamical Ejecta in the Kilonova Associated with GW170817, *Astrophys. J. Lett.* **850**, L39 (2017), [arXiv:1710.05836 \[astro-ph.HE\]](#).
  - [3] V. M. Lipunov *et al.*, MASTER Optical Detection of the First LIGO/Virgo Neutron Star Binary Merger GW170817, *Astrophys. J. Lett.* **850**, L1 (2017), [arXiv:1710.05461 \[astro-ph.HE\]](#).
  - [4] B. J. Shappee *et al.*, Early Spectra of the Gravitational Wave Source GW170817: Evolution of a Neutron Star Merger, *Science* **358**, 1574 (2017), [arXiv:1710.05432 \[astro-ph.HE\]](#).
  - [5] Y. Utsumi *et al.* (J-GEM), J-GEM observations of an electromagnetic counterpart to the neutron star merger GW170817, *Publ. Astron. Soc. Jap.* **69**, 101 (2017), [arXiv:1710.05848 \[astro-ph.HE\]](#).
  - [6] A. Goldstein *et al.*, An Ordinary Short Gamma-Ray Burst with Extraordinary Implications: Fermi-GBM Detection of GRB 170817A, *Astrophys. J. Lett.* **848**, L14 (2017), [arXiv:1710.05446 \[astro-ph.HE\]](#).
  - [7] B. P. Abbott *et al.* (LIGO Scientific, Virgo, Fermi-GBM, INTEGRAL), Gravitational Waves and Gamma-rays from a Binary Neutron Star Merger: GW170817 and GRB 170817A, *Astrophys. J. Lett.* **848**, L13 (2017), [arXiv:1710.05834 \[astro-ph.HE\]](#).
  - [8] B. P. Abbott *et al.* (LIGO Scientific, Virgo, Fermi GBM, INTEGRAL, IceCube, AstroSat Cadmium Zinc Telluride Imager Team, IPN, Insight-Hxmt, ANTARES, Swift, AGILE Team, 1M2H Team, Dark Energy Camera GW-EM, DES, DLT40, GRAWITA, Fermi-LAT, ATCA, ASKAP, Las Cumbres Observatory Group, OzGrav, DWF (Deeper Wider Faster Program), AST3, CAASTRO, VINROUGE, MASTER, J-GEM, GROWTH, JAGWAR, CaltechNRAO, TTU-NRAO, NuSTAR, Pan-STARRS, MAXI Team, TZAC Consortium, KU, Nordic Optical Telescope, ePESSTO, GROND, Texas Tech University, SALT Group, TOROS, BOOTES, MWA, CALET, IKI-GW Follow-up, H.E.S.S., LOFAR, LWA, HAWC, Pierre Auger, ALMA, Euro VLBI Team, Pi of Sky, Chandra Team at McGill University, DFN, ATLAS Telescopes, High Time Resolution Universe Survey, RIMAS, RATIR, SKA South Africa/MeerKAT), Multi-messenger Observations of a Binary Neutron Star Merger, *Astrophys. J. Lett.* **848**, L12 (2017), [arXiv:1710.05833 \[astro-ph.HE\]](#).
  - [9] P. S. Cowperthwaite *et al.*, The Electromagnetic Counterpart of the Binary Neutron Star Merger LIGO/Virgo GW170817. II. UV, Optical, and Near-infrared Light Curves and Comparison to Kilonova Models, *Astrophys. J. Lett.* **848**, L17 (2017), [arXiv:1710.05840 \[astro-ph.HE\]](#).
  - [10] J. S. Read, C. Markakis, M. Shibata, K. Uryu, J. D. E. Creighton, and J. L. Friedman, Measuring the neutron star equation of state with gravitational wave observations, *Phys. Rev. D* **79**, 124033 (2009), [arXiv:0901.3258 \[gr-qc\]](#).
  - [11] B. D. Metzger, Kilonovae, *Living Rev. Rel.* **23**, 1 (2020), [arXiv:1910.01617 \[astro-ph.HE\]](#).
  - [12] B. P. Abbott *et al.* (The LIGO Scientific Collaboration and the Virgo Collaboration), Gw170817: Measurements of neutron star radii and equation of state, *Phys. Rev. Lett.* **121**, 161101 (2018).
  - [13] B. P. Abbott *et al.* (LIGO Scientific, Virgo), GW190425: Observation of a Compact Binary Coalescence with Total Mass  $\sim 3.4M_{\odot}$ , *Astrophys. J. Lett.* **892**, L3 (2020), [arXiv:2001.01761 \[astro-ph.HE\]](#).
  - [14] R. Dudi, A. Adhikari, B. Brügmann, T. Dietrich, K. Hayashi, K. Kawaguchi, K. Kiuchi, K. Kyutoku, M. Shibata, and W. Tichy, Investigating GW190425 with numerical-relativity simulations, *Phys. Rev. D* **106**, 084039 (2022), [arXiv:2109.04063 \[astro-ph.HE\]](#).

- [15] M. C. Miller *et al.*, PSR J0030+0451 Mass and Radius from *NICER* Data and Implications for the Properties of Neutron Star Matter, *Astrophys. J. Lett.* **887**, L24 (2019), [arXiv:1912.05705 \[astro-ph.HE\]](#).
- [16] M. C. Miller *et al.*, The Radius of PSR J0740+6620 from *NICER* and *XMM-Newton* Data, *Astrophys. J. Lett.* **918**, L28 (2021), [arXiv:2105.06979 \[astro-ph.HE\]](#).
- [17] T. E. Riley *et al.*, A *NICER* View of PSR J0030+0451: Millisecond Pulsar Parameter Estimation, *Astrophys. J. Lett.* **887**, L21 (2019), [arXiv:1912.05702 \[astro-ph.HE\]](#).
- [18] T. E. Riley *et al.*, A *NICER* View of the Massive Pulsar PSR J0740+6620 Informed by Radio Timing and *XMM-Newton* Spectroscopy, *Astrophys. J. Lett.* **918**, L27 (2021), [arXiv:2105.06980 \[astro-ph.HE\]](#).
- [19] G. Raaijmakers *et al.*, Constraining the dense matter equation of state with joint analysis of *NICER* and *LIGO/Virgo* measurements, *Astrophys. J. Lett.* **893**, L21 (2020), [arXiv:1912.11031 \[astro-ph.HE\]](#).
- [20] J. Antoniadis *et al.*, A Massive Pulsar in a Compact Relativistic Binary, *Science* **340**, 6131 (2013), [arXiv:1304.6875 \[astro-ph.HE\]](#).
- [21] E. Fonseca *et al.*, Refined Mass and Geometric Measurements of the High-mass PSR J0740+6620, *Astrophys. J. Lett.* **915**, L12 (2021), [arXiv:2104.00880 \[astro-ph.HE\]](#).
- [22] R. W. Romani, D. Kandel, A. V. Filippenko, T. G. Brink, and W. Zheng, PSR J1810+1744: Companion Darkening and a Precise High Neutron Star Mass, *Astrophys. J. Lett.* **908**, L46 (2021), [arXiv:2101.09822 \[astro-ph.HE\]](#).
- [23] R. W. Romani, D. Kandel, A. V. Filippenko, T. G. Brink, and W. Zheng, PSR J0952–0607: The Fastest and Heaviest Known Galactic Neutron Star, *Astrophys. J. Lett.* **934**, L18 (2022), [arXiv:2207.05124 \[astro-ph.HE\]](#).
- [24] J. Nättilä, M. C. Miller, A. W. Steiner, J. J. E. Kajava, V. F. Suleimanov, and J. Poutanen, Neutron star mass and radius measurements from atmospheric model fits to X-ray burst cooling tail spectra, *Astron. Astrophys.* **608**, A31 (2017), [arXiv:1709.09120 \[astro-ph.HE\]](#).
- [25] A. J. Goodwin, D. K. Galloway, A. Heger, A. Cumming, and Z. Johnston, A Bayesian Approach to Matching Thermonuclear X-ray Burst Observations with Models, *Mon. Not. Roy. Astron. Soc.* **490**, 2228 (2019), [arXiv:1907.00996 \[astro-ph.HE\]](#).
- [26] H. Koehn, H. Rose, P. T. H. Pang, R. Somasundaram, B. T. Reed, I. Tews, A. Abac, O. Komoltsev, N. Kunert, A. Kurkela, M. W. Coughlin, B. F. Healy, and T. Dietrich, From existing and new nuclear and astrophysical constraints to stringent limits on the equation of state of neutron-rich dense matter, *Phys. Rev. X* **15**, 021014 (2025), [arXiv:2402.04172 \[astro-ph.HE\]](#).
- [27] G. Panotopoulos and I. Lopes, Dark matter effect on realistic equation of state in neutron stars, *Phys. Rev. D* **96**, 083004 (2017), [arXiv:1709.06312 \[hep-ph\]](#).
- [28] A. G. Abac, C. C. Bernido, and J. P. H. Esguerra, Stability of neutron stars with dark matter core using three crustal types and the impact on mass–radius relations, *Phys. Dark Univ.* **40**, 101185 (2023), [arXiv:2104.04969 \[nucl-th\]](#).
- [29] E. Giangrandi, V. Sagun, O. Ivanytskyi, C. Providência, and T. Dietrich, The Effects of Self-interacting Bosonic Dark Matter on Neutron Star Properties, *Astrophys. J.* **953**, 115 (2023), [arXiv:2209.10905 \[astro-ph.HE\]](#).
- [30] M. Hippert, E. Dillingham, H. Tan, D. Curtin, J. Noronha-Hostler, and N. Yunes, Dark matter or regular matter in neutron stars? How to tell the difference from the coalescence of compact objects, *Phys. Rev. D* **107**, 115028 (2023), [arXiv:2211.08590 \[astro-ph.HE\]](#).
- [31] R. F. Dieckrichs, N. Becker, C. Jockel, J.-E. Christian, L. Sagunski, and J. Schaffner-Bielich, Tidal deformability of fermion-boson stars: Neutron stars admixed with ultralight dark matter, *Phys. Rev. D* **108**, 064009 (2023), [arXiv:2303.04089 \[gr-qc\]](#).
- [32] E. Giangrandi, A. Ávila, V. Sagun, O. Ivanytskyi, and C. Providência, The Impact of Asymmetric Dark Matter on the Thermal Evolution of Nucleonic and Hyperonic Compact Stars, *Particles* **7**, 179 (2024), [arXiv:2401.03295 \[astro-ph.HE\]](#).
- [33] O. Ivanytskyi, V. Sagun, and I. Lopes, Neutron stars: New constraints on asymmetric dark matter, *Phys. Rev. D* **102**, 063028 (2020), [arXiv:1910.09925 \[astro-ph.HE\]](#).
- [34] J. Ellis, A. Hektor, G. Hütsi, K. Kannike, L. Marzola, M. Raidal, and V. Vaskonen, Search for Dark Matter Effects on Gravitational Signals from Neutron Star Mergers, *Phys. Lett. B* **781**, 607 (2018), [arXiv:1710.05540 \[astro-ph.CO\]](#).
- [35] J. Stadel, D. Potter, B. Moore, J. Diemand, P. Madau, M. Zemp, M. Kuhlen, and V. Quilis, Quantifying the heart of darkness with *GHALO* - a multi-billion particle simulation of our galactic halo, *Mon. Not. Roy. Astron. Soc.* **398**, L21 (2009), [arXiv:0808.2981 \[astro-ph\]](#).
- [36] M. Weber and W. de Boer, Determination of the Local Dark Matter Density in our Galaxy, *Astron. Astrophys.* **509**, A25 (2010), [arXiv:0910.4272 \[astro-ph.CO\]](#).
- [37] C. Kouvaris and P. Tinyakov, Can Neutron stars constrain Dark Matter?, *Phys. Rev. D* **82**, 063531 (2010), [arXiv:1004.0586 \[astro-ph.GA\]](#).
- [38] M. Bezares, D. Viganò, and C. Palenzuela, Gravitational wave signatures of dark matter cores in binary neutron star mergers by using numerical simulations, *Phys. Rev. D* **100**, 044049 (2019), [arXiv:1905.08551 \[gr-qc\]](#).
- [39] A. Bauswein, G. Guo, J.-H. Lien, Y.-H. Lin, and M.-R. Wu, Compact dark objects in neutron star mergers, *Phys. Rev. D* **107**, 083002 (2023), [arXiv:2012.11908 \[astro-ph.HE\]](#).
- [40] M. Emma, F. Schianchi, F. Pannarale, V. Sagun, and T. Dietrich, Numerical Simulations of Dark Matter Admixed Neutron Star Binaries, *Particles* **5**, 273 (2022), [arXiv:2206.10887 \[gr-qc\]](#).
- [41] H. R. Rüter, V. Sagun, W. Tichy, and T. Dietrich, Quasiequilibrium configurations of binary systems of dark matter admixed neutron stars, *Phys. Rev. D* **108**, 124080 (2023), [arXiv:2301.03568 \[gr-qc\]](#).
- [42] W. Tichy, A New numerical method to construct binary neutron star initial data, *Class. Quant. Grav.* **26**, 175018 (2009), [arXiv:0908.0620 \[gr-qc\]](#).
- [43] W. Tichy, Constructing quasi-equilibrium initial data for binary neutron stars with arbitrary spins, *Phys. Rev. D* **86**, 064024 (2012), [arXiv:1209.5336 \[gr-qc\]](#).
- [44] T. Dietrich, N. Moldenhauer, N. K. Johnson-McDaniel, S. Bernuzzi, C. M. Markakis, B. Brügmann, and W. Tichy, Binary Neutron Stars with Generic Spin, Eccentricity, Mass ratio, and Compactness - Quasiequilibrium Sequences and First Evolutions, *Phys. Rev. D* **92**, 124007 (2015), [arXiv:1507.07100 \[gr-qc\]](#).
- [45] W. Tichy, A. Rashti, T. Dietrich, R. Dudi, and

- B. Brügmann, Constructing binary neutron star initial data with high spins, high compactnesses, and high mass ratios, *Phys. Rev. D* **100**, 124046 (2019), [arXiv:1910.09690 \[gr-qc\]](#).
- [46] C. B. Owen, A. Tucker, Y. Kahn, and N. Yunes, Constraining dark-sector effects using gravitational waves from compact binary inspirals (2025), [arXiv:2503.04916 \[gr-qc\]](#).
- [47] D. Suárez-Fontanella, D. Barba-González, C. Albertus, and M. A. Pérez-García, Gravitational wave emission in binary neutron star early post-merger within a dark environment, *Phys. Lett. B* **862**, 139358 (2025), [arXiv:2408.05226 \[gr-qc\]](#).
- [48] M. Branchesi *et al.*, Science with the Einstein Telescope: a comparison of different designs, *JCAP* **2023** (07), 068, [arXiv:2303.15923 \[gr-qc\]](#).
- [49] M. Punturo *et al.*, The Einstein Telescope: A third-generation gravitational wave observatory, *Class. Quant. Grav.* **27**, 194002 (2010).
- [50] A. Abac *et al.*, The Science of the Einstein Telescope (2025), [arXiv:2503.12263 \[gr-qc\]](#).
- [51] D. Reitze *et al.*, The US program in ground-based gravitational wave science: Contribution from the LIGO laboratory, *Bull. Am. Astron. Soc.* **51**, 141 (2019), [arXiv:1903.04615 \[astro-ph.IM\]](#).
- [52] D. Reitze *et al.*, Cosmic Explorer: The U.S. Contribution to Gravitational-Wave Astronomy beyond LIGO, *Bull. Am. Astron. Soc.* **51**, 035 (2019), [arXiv:1907.04833 \[astro-ph.IM\]](#).
- [53] K. Ackley *et al.*, Neutron Star Extreme Matter Observatory: A kilohertz-band gravitational-wave detector in the global network, *Publ. Astron. Soc. Austral.* **37**, e047 (2020), [arXiv:2007.03128 \[astro-ph.HE\]](#).
- [54] L. Roszkowski, E. M. Sessolo, and S. Trojanowski, WIMP dark matter candidates and searches—current status and future prospects, *Rept. Prog. Phys.* **81**, 066201 (2018), [arXiv:1707.06277 \[hep-ph\]](#).
- [55] M. Pospelov, A. Ritz, and M. B. Voloshin, Secluded WIMP Dark Matter, *Phys. Lett. B* **662**, 53 (2008), [arXiv:0711.4866 \[hep-ph\]](#).
- [56] R. Foot, Mirror dark matter: Cosmology, galaxy structure and direct detection, *Int. J. Mod. Phys. A* **29**, 1430013 (2014), [arXiv:1401.3965 \[astro-ph.CO\]](#).
- [57] D. Paraficz, J. P. Kneib, J. Richard, A. Morandi, M. Limousin, E. Jullo, and J. Martinez, The Bullet cluster at its best: weighing stars, gas, and dark matter, *Astron. Astrophys.* **594**, A121 (2016), [arXiv:1209.0384 \[astro-ph.CO\]](#).
- [58] A. Robertson, R. Massey, and V. Eke, What does the Bullet Cluster tell us about self-interacting dark matter?, *Mon. Not. Roy. Astron. Soc.* **465**, 569 (2017), [arXiv:1605.04307 \[astro-ph.CO\]](#).
- [59] J. Aalbers *et al.* (LZ), First Dark Matter Search Results from the LUX-ZEPLIN (LZ) Experiment, *Phys. Rev. Lett.* **131**, 041002 (2023), [arXiv:2207.03764 \[hep-ex\]](#).
- [60] E. Aprile *et al.* (XENON), First Dark Matter Search with Nuclear Recoils from the XENONnT Experiment, *Phys. Rev. Lett.* **131**, 041003 (2023), [arXiv:2303.14729 \[hep-ex\]](#).
- [61] O. Ivanytskyi, V. Sagun, and I. Lopes, Neutron stars: New constraints on asymmetric dark matter, *Phys. Rev. D* **102**, 063028 (2020), [arXiv:1910.09925 \[astro-ph.HE\]](#).
- [62] D. Rafiei Karkevandi, S. Shakeri, V. Sagun, and O. Ivanytskyi, Bosonic dark matter in neutron stars and its effect on gravitational wave signal, *Phys. Rev. D* **105**, 023001 (2022), [arXiv:2109.03801 \[astro-ph.HE\]](#).
- [63] J. W. York, Jr., Conformal 'thin sandwich' data for the initial-value problem, *Phys. Rev. Lett.* **82**, 1350 (1999), [arXiv:gr-qc/9810051](#).
- [64] H. P. Pfeiffer and J. W. York, Jr., Extrinsic curvature and the Einstein constraints, *Phys. Rev. D* **67**, 044022 (2003), [arXiv:gr-qc/0207095](#).
- [65] T. W. Baumgarte and S. L. Shapiro, *Numerical Relativity: Solving Einstein's Equations on the Computer* (Cambridge University Press, 2010).
- [66] W. Tichy, The initial value problem as it relates to numerical relativity, *Rept. Prog. Phys.* **80**, 026901 (2017), [arXiv:1610.03805 \[gr-qc\]](#).
- [67] N. Moldenhauer, C. M. Markakis, N. K. Johnson-McDaniel, W. Tichy, and B. Brügmann, Initial data for binary neutron stars with adjustable eccentricity, *Phys. Rev. D* **90**, 084043 (2014), [arXiv:1408.4136 \[gr-qc\]](#).
- [68] C. Runge, Über empirische funktionen und die interpolation zwischen äquidistanten ordinaten, *Zeitschrift für Mathematik und Physik* **46**, 224 (1901).
- [69] B. Brügmann, J. A. González, M. Hannam, S. Husa, U. Sperhake, and W. Tichy, Calibration of moving puncture simulations, *Phys. Rev. D* **77**, 024027 (2008), [arXiv:gr-qc/0610128](#).
- [70] M. Thierfelder, S. Bernuzzi, and B. Brügmann, Numerical relativity simulations of binary neutron stars, *Phys. Rev. D* **84**, 044012 (2011), [arXiv:1104.4751 \[gr-qc\]](#).
- [71] T. Dietrich, S. Bernuzzi, M. Ujevic, and B. Brügmann, Numerical relativity simulations of neutron star merger remnants using conservative mesh refinement, *Phys. Rev. D* **91**, 124041 (2015), [arXiv:1504.01266 \[gr-qc\]](#).
- [72] S. Bernuzzi and T. Dietrich, Gravitational waveforms from binary neutron star mergers with high-order weighted-essentially-noscillatory schemes in numerical relativity, *Phys. Rev. D* **94**, 064062 (2016), [arXiv:1604.07999 \[gr-qc\]](#).
- [73] T. Dietrich, D. Radice, S. Bernuzzi, F. Zappa, A. Perego, B. Brügmann, S. V. Chaurasia, R. Dudi, W. Tichy, and M. Ujevic, CoRe database of binary neutron star merger waveforms, *Class. Quant. Grav.* **35**, 24LT01 (2018), [arXiv:1806.01625 \[gr-qc\]](#).
- [74] A. Neuweiler, T. Dietrich, B. Brügmann, E. Giangrandi, K. Kiuchi, F. Schianchi, P. Mösta, S. Shankar, B. Giacomazzo, and M. Shibata, General relativistic magnetohydrodynamic simulations with bam: Implementation and code comparison, *Phys. Rev. D* **110**, 084046 (2024), [arXiv:2407.20946 \[gr-qc\]](#).
- [75] H. Gieg, F. Schianchi, M. Ujevic, and T. Dietrich, On the Role of Muons in Binary Neutron Star Mergers: First Simulations (2024), [arXiv:2409.04420 \[gr-qc\]](#).
- [76] F. Schianchi, H. Gieg, V. Nedora, A. Neuweiler, M. Ujevic, M. Bulla, and T. Dietrich, M1 neutrino transport within the numerical-relativistic code BAM with application to low mass binary neutron star mergers, *Phys. Rev. D* **109**, 044012 (2024), [arXiv:2307.04572 \[gr-qc\]](#).
- [77] C. Bona, T. Ledvinka, C. Palenzuela, and M. Zacek, General covariant evolution formalism for numerical relativity, *Phys. Rev. D* **67**, 104005 (2003), [arXiv:gr-qc/0302083](#).
- [78] C. Bona, L. Lehner, and C. Palenzuela-Luque, Geometrically motivated hyperbolic coordinate conditions for numerical relativity: Analysis, issues and imple-

- mentations, *Phys. Rev. D* **72**, 104009 (2005), [arXiv:gr-qc/0509092](#).
- [79] C. Gundlach, J. M. Martin-Garcia, G. Calabrese, and I. Hinder, Constraint damping in the Z4 formulation and harmonic gauge, *Class. Quant. Grav.* **22**, 3767 (2005), [arXiv:gr-qc/0504114](#).
- [80] S. Bernuzzi and D. Hilditch, Constraint violation in free evolution schemes: Comparing BSSNOK with a conformal decomposition of Z4, *Phys. Rev. D* **81**, 084003 (2010), [arXiv:0912.2920 \[gr-qc\]](#).
- [81] D. Hilditch, S. Bernuzzi, M. Thierfelder, Z. Cao, W. Tichy, and B. Brügmann, Compact binary evolutions with the z4c formulation, *Phys. Rev. D* **88**, 084057 (2013), [arXiv:1212.2901 \[gr-qc\]](#).
- [82] M. Alcubierre, B. Brügmann, P. Diener, M. Koppitz, D. Pollney, E. Seidel, and R. Takahashi, Gauge conditions for long-term numerical black hole evolutions without excision, *Phys. Rev. D* **67**, 084023 (2003), [arXiv:gr-qc/0206072](#).
- [83] F. Banyuls, J. A. Font, J. M. Ibáñez, J. M. Martí, and J. A. Miralles, Numerical  $\{3 + 1\}$  General Relativistic Hydrodynamics: A Local Characteristic Approach, *Astrophys. J.* **476**, 221 (1997).
- [84] F. Gulminelli and A. R. Raduta, Unified treatment of subsaturation stellar matter at zero and finite temperature, *Phys. Rev. C* **92**, 055803 (2015), [arXiv:1504.04493 \[nucl-th\]](#).
- [85] B. P. Abbott *et al.* (LIGO Scientific, Virgo), GW170817: Measurements of neutron star radii and equation of state, *Phys. Rev. Lett.* **121**, 161101 (2018), [arXiv:1805.11581 \[gr-qc\]](#).
- [86] A. Bauswein, H. T. Janka, and R. Oechslin, Testing Approximations of Thermal Effects in Neutron Star Merger Simulations, *Phys. Rev. D* **82**, 084043 (2010), [arXiv:1006.3315 \[astro-ph.SR\]](#).
- [87] T. Zwerger and E. Müller, Dynamics and gravitational wave signature of axisymmetric rotational core collapse, *Astron. Astrophys.* **320**, 209 (1997).
- [88] V. Sagun, E. Giangrandi, O. Ivanytskyi, I. Lopes, and K. A. Bugaev, Constraints on the fermionic dark matter from observations of neutron stars, *PoS PANIC2021*, 313 (2022), [arXiv:2111.13289 \[astro-ph.HE\]](#).
- [89] L. Rezzolla and O. Zanotti, *Relativistic Hydrodynamics* (Oxford University Press, 2013).
- [90] L. Baiotti and L. Rezzolla, Binary neutron star mergers: a review of Einstein's richest laboratory, *Rept. Prog. Phys.* **80**, 096901 (2017), [arXiv:1607.03540 \[gr-qc\]](#).
- [91] T. Dietrich, S. Ossokine, and K. Clough, Full 3D numerical relativity simulations of neutron star–boson star collisions with BAM, *Class. Quant. Grav.* **36**, 025002 (2019), [arXiv:1807.06959 \[gr-qc\]](#).
- [92] M. Berger and P. Colella, Local adaptive mesh refinement for shock hydrodynamics, *Journal of Computational Physics* **82**, 64 (1989).
- [93] M. J. Berger and J. Olinger, Adaptive mesh refinement for hyperbolic partial differential equations, *Journal of Computational Physics* **53**, 484 (1984).
- [94] R. Borges, M. Carmona, B. Costa, and W. S. Don, An improved weighted essentially non-oscillatory scheme for hyperbolic conservation laws, *Journal of Computational Physics* **227**, 3191 (2008).
- [95] A. Das, T. Malik, and A. C. Nayak, Dark matter admixed neutron star properties in light of gravitational wave observations: A two fluid approach, *Phys. Rev. D* **105**, 123034 (2022), [arXiv:2011.01318 \[nucl-th\]](#).
- [96] T. Hinderer, Tidal love numbers of neutron stars, *The Astrophysical Journal* **677**, 1216 (2008).
- [97] K.-L. Leung, M.-c. Chu, and L.-M. Lin, Tidal deformability of dark matter admixed neutron stars, *Phys. Rev. D* **105**, 123010 (2022), [arXiv:2207.02433 \[astro-ph.HE\]](#).
- [98] M. Hanauske, K. Takami, L. Bovard, L. Rezzolla, J. A. Font, F. Galeazzi, and H. Stöcker, Rotational properties of hypermassive neutron stars from binary mergers, *Phys. Rev. D* **96**, 043004 (2017), [arXiv:1611.07152 \[gr-qc\]](#).
- [99] K. Hotokezaka, K. Kiuchi, K. Kyutoku, H. Okawa, Y.-i. Sekiguchi, M. Shibata, and K. Taniguchi, Mass ejection from the merger of binary neutron stars, *Phys. Rev. D* **87**, 024001 (2013), [arXiv:1212.0905 \[astro-ph.HE\]](#).
- [100] A. Abac, T. Dietrich, A. Buonanno, J. Steinhoff, and M. Ujevic, New and robust gravitational-waveform model for high-mass-ratio binary neutron star systems with dynamical tidal effects, *Phys. Rev. D* **109**, 024062 (2024), [arXiv:2311.07456 \[gr-qc\]](#).
- [101] LIGO Scientific Collaboration, *LIGO Algorithm Library - LALSuite*, free software (GPL) (2018).
- [102] G. Pratten, S. Husa, C. Garcia-Quiros, M. Colleoni, A. Ramos-Buades, H. Estelles, and R. Jaume, Setting the cornerstone for a family of models for gravitational waves from compact binaries: The dominant harmonic for nonprecessing quasicircular black holes, *Phys. Rev. D* **102**, 064001 (2020), [arXiv:2001.11412 \[gr-qc\]](#).
- [103] T. Dietrich, S. Bernuzzi, and W. Tichy, Closed-form tidal approximants for binary neutron star gravitational waveforms constructed from high-resolution numerical relativity simulations, *Phys. Rev. D* **96**, 121501 (2017), [arXiv:1706.02969 \[gr-qc\]](#).
- [104] T. Dietrich *et al.*, Matter imprints in waveform models for neutron star binaries: Tidal and self-spin effects, *Phys. Rev. D* **99**, 024029 (2019), [arXiv:1804.02235 \[gr-qc\]](#).
- [105] T. Dietrich, A. Samajdar, S. Khan, N. K. Johnson-McDaniel, R. Dudi, and W. Tichy, Improving the NR-Tidal model for binary neutron star systems, *Phys. Rev. D* **100**, 044003 (2019), [arXiv:1905.06011 \[gr-qc\]](#).
- [106] K. Hotokezaka, K. Kyutoku, H. Okawa, and M. Shibata, Exploring tidal effects of coalescing binary neutron stars in numerical relativity. II. Long-term simulations, *Phys. Rev. D* **91**, 064060 (2015), [arXiv:1502.03457 \[gr-qc\]](#).
- [107] A. Nelson, S. Reddy, and D. Zhou, Dark halos around neutron stars and gravitational waves, *JCAP* **07**, 012, [arXiv:1803.03266 \[hep-ph\]](#).
- [108] H.-M. Liu, J.-B. Wei, Z.-H. Li, G. F. Burgio, H. C. Das, and H. J. Schulze, Dark matter effects on the properties of neutron stars: Compactness and tidal deformability, *Phys. Rev. D* **110**, 023024 (2024), [arXiv:2403.17024 \[nucl-th\]](#).
- [109] H. Sotani and B. Kumar, Universal relations between the quasinormal modes of neutron star and tidal deformability, *Phys. Rev. D* **104**, 123002 (2021), [arXiv:2109.08145 \[gr-qc\]](#).